www.czasopisma.pan.pl PAN www.journals.pan.pl

ARCHIVES OF ACOUSTICS
Vol. **42**, No. 4, pp. 653–675 (2017)

DOI: 10.1515/aoa-2017-0069

Numerical Prediction of the Tonal Airborne Noise for a NACA 0012 Aerofoil at Moderate Reynolds Number Using a Transitional URANS Approach

Michele DE GENNARO, Helmut KÜHNELT, Alessandro ZANON

AIT, Austrian Institute of Technology GmbH, Center for Low-Emission Transport
Giefinggasse 2, Vienna, 1210, Austria; e-mail: {michele.degennaro, helmut.kuehnelt, alessandro.zanon}@ait.ac.at

(*received April 7, 2016; accepted May 17, 2017*)

Tonal airborne noise of aerofoils appears in a limited range of moderate Reynolds numbers and angles of attack. In these specific conditions, the aerofoil is characterised by a large region of laminar flow over the aerodynamic surface, typically resulting in two-dimensional laminar instabilities in the boundary layer, generating one or more acoustic tones. The numerical simulation of such phenomenon requires, beside an accurate prediction of the unsteady flow field, a proper modelling of the laminar to turbulent transition of the boundary layer, which generally imposes the use of highly CPU demanding approaches such as large eddy simulation (LES) or direct numerical simulation (DNS). This paper aims at presenting the results of numerical experiments for evaluating the capability of capturing the tonal airborne noise by using an advanced, yet low computationally demanding, unsteady Reynolds-averaged Navier-Stokes (URANS) turbulence model augmented with a transitional model to account for the laminar to turbulent transition. This approach, coupled with the Ffowcs Williams and Hawkings (FW-H) acoustic analogy, is adopted for predicting the far-field acoustic sound pressure of a NACA 0012 aerofoil with Reynolds number ranging from $0.39 \cdot 10^6$ to $1.09 \cdot 10^6$. The results show a main tone located approximately at 1.6–1.8 kHz for a Reynolds number equal to $0.62 \cdot 10^6$, increasing to 2.4 kHz at Reynolds number equal to $0.85 \cdot 10^6$ and 3.4 kHz at $1.09 \cdot 10^6$, while no main tones are observed at $0.39 \cdot 10^6$. The computed spectra confirm that the acoustic emission of the aerofoil is dominated by tonal structures and that the frequency of the main tone depends on the Reynolds number consistently with the ladder-like tonal structure suggested by Paterson *et al.* Moreover, in specific conditions, the acoustic spectra exhibit a multi-tonal structure visible in narrowband spectra, in line with the findings of Arbey and Bataille. The presented results demonstrate the capability of the numerical model of predicting the physics of the tonal airborne noise generation.

Keywords: tonal airborne noise; NACA 0012; Laminar Boundary Layer-Vortex Shedding noise; ladder-like tonal structure of the acoustic spectrum; multi-tonal structure of the acoustic spectrum.

Nomenclature

a – speed of sound,
A, A', B, $K_{1,2}$, ΔK_1,$G_{1,2,3}$ – Brooks-Pope-Marcolini model semi-empirical functions,
c – chord length,
$D_{h,l}$ – correction coefficients accounting for the effect of the noise directivity,
E, P – k-ω transitional turbulence model sources,
f_s – main tone frequency according to Paterson *et al.*,
F, Q – FW-H additional sources,
H – Heaviside function,
k, m – Arbey and Bataille coefficients for the secondary tones formula,
L – span wise dimension of the aerofoil,
L_A – distance between the point of maximum velocity over the aerofoil and the trailing edge,
M, M_c – Mach number of the flow and of the flow downstream the trailing edge of the aerofoil,
p, p' – pressure, acoustic pressure,
Re, $\mathrm{Re}_{\theta t}$ – Reynolds number, momentum thickness Reynolds number,
r_e – distance between the trailing edge at the receiver location,
S – semi-span size of the aerofoil model (dimensional),
St – Strouhal number,
$\underline{\underline{T}}$, T_{ij} – Lighthill's tensor,
t – time,
V – asymptotic flow speed,
$\mathbf{v}$, v_i – velocity (vector and i-th component),
$\mathbf{x}$, x_i – position (vector and i-th component),
$x[i]$ – discrete signal,
α^* – angle of attack,
γ – intermittency,
δ – boundary layer thickness,

δ^* – displacement thickness of the boundary layer,
δ' – Dirac delta function,
Θ_ε – longitudinal view angle of the receiver with respect to the trailing edge of the aerofoil,
ξ – generic volume coordinates,
μ – dynamic viscosity,
ρ, ρ' – fluid density, acoustic density,
σ_{ij} – viscosity stress tensor (i, j-th component),
τ_{ij} – turbulence stress tensor (i, j-th component),
υ – kinematic viscosity,
Φ_ε – latitudinal view angle of the receiver with respect to the trailing edge of the aerofoil.

Acronyms

BPM – Brooks-Pope-Marcolini semi-empirical model,
CAA – Computational Aeroacoustics,
CFD – Computational Fluid Dynamics,
DES – Detached Eddy Simulation,
DFT – Discrete Fourier Transform,
FFT – Fast Fourier Transform,
FW-H – Ffowcs Williams and Hawkings,
LBL-VS – Laminar Boundary Layer-Vortex Shedding,
LES – Large Eddy Simulation,
NACA – National Advisory Committee for Aeronautics,
PSDL – Power Spectral Density Level,
QUICK – Quadratic upwind differencing scheme,
RANS – Reynolds Averaged Navier-Stokes,
S-S – Separation-Stall,
SAS – Scale Adaptive Simulation,
SIMPLE – Semi-Implicit Method for Pressure Linked Equations,
SST – Shear Stress Transport (referred to the k-ω turbulence model),
T-S – Tollmien-Schlichting,
TBL-TE(-P/S) – Turbulent Boundary Layer-Trailing Edge (Pressure/Suction contribution),
URANS – Unsteady RANS.

1. Introduction

Aerodynamic noise of aerofoils is a topic of interest for many engineering applications, in the frame of aeronautics, vehicle industry, ventilation systems and wind energy. This field has seen the increasing adoption of Computational Fluid Dynamics (CFD) and Computational Aeroacoustics (CAA) techniques over the last decade, thanks to the significant advancement of the numerical models and the increasing affordability of computational facilities. However the high complexity of the small scales turbulent phenomena which regulate the diverse airborne noise generation mechanisms makes this problem difficult to be approached with simplified models, therefore often more computational-intensive approaches, such as Large Eddy Simulation (LES) or Direct Navier-Stokes (DNS) simulation, have been adopted.

As far as noise from isolated aerofoils is concerned, a comprehensive classification was presented by Brooks *et al.* (1989). They classified the airborne noise from a NACA 0012 aerofoil in isolated configuration and for diverse Reynolds numbers in three main generation mechanisms:

- Turbulent Boundary Layer – Trailing Edge (TBL-TE) noise;
- Laminar Boundary Layer – Vortex Shedding (LBL-VS) noise;
- Separation – Stall (S-S) noise.

The TBL-TE mechanism (Fig. 1a) occurs when a large region of turbulent boundary layer appears on the surface, and it can be ascribed to the turbulence, typically resulting in a broadband noise spectrum. The LBL-VS mechanism (Fig. 1b) occurs when the laminar instabilities appear on the aerodynamic surface, establishing flow fluctuations, resulting in a tonal noise. On the other hand, when the flow is characterized by large regions of separation, the vortex structures are generated (e.g. Von Karman vortices) and the S-S mechanism occurs (Fig. 1c), resulting in one or more tones superimposed to a broadband noise spectrum. Additional noise generation mechanisms, not included in these cases, can exist under particular circumstances, such as blunt trailing edge of the aerofoil (i.e. bluntness noise), wing-tip vortex release (i.e. three-dimensional effects) and high level of asymptotic turbulence (i.e. free-stream turbulence noise). From the physical point of view, the TBL-TE and S-S are respectively related to the boundary layer turbulence and to the stall flow separation, therefore

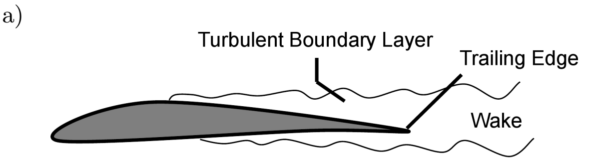

Turbulent Boundary Layer – Trailing Edge Noise

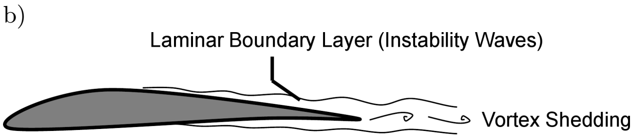

Laminar Boundary Layer – Vortex Shedding Noise

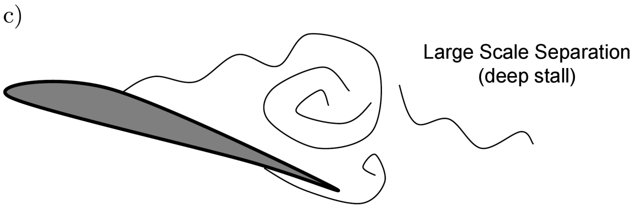

Separation Stall Noise

Fig. 1. Noise generation mechanisms classification. Turbulent B.L. – Trailing Edge (a), Laminar B.L. – Vortex Shedding (b) and Separation-Stall (c), as per (Brooks *et al.*, 1989).

the correct prediction of the generated noise necessarily requires the ability to deal with the resolution of the turbulent scales in the flow field. Several studies have been carried out on this topic, by applying the Detached Eddy Simulation (DES), the LES and the DNS, resulting in a prohibitive computational burden for practical applications (EWERT, SCHRÖDER, 2003; 2004; TAM, JU, 2012). Novel approaches such as the Zonal LES (DE GENNARO *el al.*, 2012) or reduced-order and semi-empirical approaches (DE GENNARO, KUEHNELT, 2011; 2012a; 2012b; FUGLSANG, MADSEN, 1996; ROZENBERG *et al.*, 2008) have been recently proposed, in order to reduce the computational resources required.

On the other hand, the LBL-VS is a phenomenon occurring at the laminar boundary layer at moderate Reynolds numbers (BROOKS *et al.*, 1989; TAM, JU, 2012; ARBEY, BATAILLE, 1983; NAKANO *et al.*, 2006; CHONG *et al.*, 2013) and characterised by a late transition-to-turbulence over the aerofoil surface. This implies that the boundary layer remains laminar over most of the aerodynamic surface, generating laminar instability waves that propagate in the direction of the flow. In 1973, PATERSON *et al.* (1973) investigated this phenomenon in an open wind tunnel using primarily a NACA 0012 aerofoil. They found that the frequencies of the tones depend on the flow velocity and Angle of Attack (i.e. AoA), showing a ladder-like structure. This ladder structure exhibits a local proportionality of the excited frequencies to the flow velocity ($\propto V^{0.8}$), while the main tone frequency f_s is proportional to $V^{1.5}$ according to Eq. (1), where V is the asymptotic flow velocity, c is the chord length of the aerofoil and υ is the kinematic viscosity of the air.

$$f_s = 0.011 V^{1.5} (c\nu)^{-0.5}. \tag{1}$$

The steps of the ladder can be predicted by varying a quantisation number, and, in most cases, the acoustic spectrum exhibits several peaks. Moreover, the surface pressure fluctuations exhibit a strong spanwise correlation, suggesting that the tones are generated by two-dimensional flow structures.

ARBEY and BATAILLE (1983) repeated the experiments from *Paterson et al.* (1983), observing a large number of tones superimposed to the broadband spectrum. They discovered that the frequency of the main tone was in agreement with Eq. (1), but the prediction of the multi-tonal structures observed requires a more complex approach. They proposed the relation (2) for the main tone frequency f_s, plus a semi-empirical relation for the secondary tones, Eq. (3):

$$f_s = \frac{\mathrm{St} \cdot V}{\delta^*}, \tag{2}$$

$$\Delta f = \frac{k V^m}{L_A}, \tag{3}$$

where St is the Strouhal number associated to the instability phenomenon (i.e. St $= 0.048 \pm 0.003$ for every Re), δ^* the displacement thickness of the boundary layer computed according to MARI *et al.* (1976), $k = 0.89 \pm 0.05$, $m = 0.85 \pm 0.01$ and L_A is the distance between the point of maximum velocity over the aerofoil surface (i.e. expansion peak, located on the suction surface) and the trailing edge. They also suggest that the diffraction of the Tollmien-Schlichting (T-S) instability waves at the trailing edge generates acoustic waves, which propagate in the far field, triggering an acoustic feedback loop whose characteristic length is equal to L_A. ARCONDOULIS *et al.* (2013) also identified a feedback loop, as results of experimental tests on the NACA 0012 in a range of Reynolds number from 50,000 to 150,000 and by PLOGMANN and WÜRZ (2013) in a wide range of angles of attack, i.e. from 0 to 8°, and free-stream velocities, i.e. from 30 to 70 m/s.

Further experimental analyses have been performed by MCALPINE *et al.* (1999) and NASH *et al.* (1999). They reproduced the setup described by (ARBEY, BATAILLE, 1983; PATERSON *et al.*, 1973) lining the walls of a wind tunnel with sound absorbing material. They found one main tone with no ladder structure, proposing that the secondary tones registered by Arbey and Bataille were spurious spectral components generated by the interference of their experimental devices with the clean flow. Therefore, they propose that no feedback loop is established, although their results are in well agreement with Eq. (1). Similarly, PRÖBSTING *et al.* (2015) identified tonal noise generation on a NACA 0012 aerofoil in a range of Reynolds number from 30,000 to 230,000 and AoA from 0 to 6.3°, although they highlight that controversy remains on the respective significance of pressure- and suction-side events, along with their interaction for tonal noise generation.

In the recent years, many authors have investigated the tonal noise generation mechanisms from aerofoils, in different conditions and for different geometries (ARCONDOULIS *et al.*, 2011; DESQUESNES *et al.*, 2007; JONES *et al.*, 2008; 2010; KUROTAKI *et al.*, 2008). Many studies agree that T-S instability waves are established and that a feedback loop mechanisms is sustained, thus generating the tone. In particular, KINGAN and PEARSE (2009) propose that the relevant length scale for this loop must be the distance between the trailing edge and the beginning of the instabilities, solving the Orr-Sommerfeld equation in this region to estimate the frequency of maximum amplification of the disturbances. DESQUESNES *et al.* (2007) applies the two-dimensional DNS, finding that the frequency of the most amplified instability wave is close to the main tone frequency for a Reynolds number equal to $0.2 \cdot 10^6$, whereas KUROTAKI *et al.* (2008) applies the LES in a range of Reynolds numbers between $0.4 \cdot 10^6$ and $0.8 \cdot 10^6$, finding a good agreement with the formula from Paterson *et al.* (1973). Jones and Sandberg (2011) and Jones *et al.* (2008; 2010) apply the DNS up to a Reynolds number of $0.1 \cdot 10^6$ to investigate the instabilities, and recently also Tam and Ju (2012) have proposed the DNS, finding a single tone in a range of Reynolds number between $0.2 \cdot 10^6$ and $0.5 \cdot 10^6$. This single tone is generated by the interaction of the oscillatory motion of the near wake driven by flow instabilities developed at the trailing edge. The two-dimensional nature of this phenomenon is further highlighted by the experimental study of Golubev *et al.* (2014), which confirms the existence of ladder-like tonal structures with single velocity dependence for the dominant spectral components.

The objective of this paper is to provide the scientific community with the results of numerical experiments targeted to predict the tonal noise of a NACA 0012 aerofoil at moderate Reynolds number flow regime. The flow solution is computed by solving the two-dimensional compressible URANS equations with the *k-ω SST* transitional turbulence model (Menter, 1994; Menter *et al.*, 2004), whereas the far-field acoustic sound pressure is computed with the Ffowcs-Williams and Hawkings (FW-H) acoustic analogy (Brentner, Farassat, 1998; Ffowcs-Williams, Hawkings, 1969).

The innovativeness of the present work consists in proposing, for the first time, the simulation of the airborne tonal noise generation mechanisms with a relatively low computational CPU demanding approach. The two-dimensional nature of this phenomenon, the laminar instabilities and the late transition-to-turbulence are well captured by the present model, allowing accurate and quick predictions of the acoustic spectrum over a vast range of Reynolds numbers.

The testing conditions account for two AoAs (i.e. 4 and 5°) and Reynolds numbers of the asymptotic flow ranging from $0.39 \cdot 10^6$ to $1.09 \cdot 10^6$. The simulations are performed with the commercial software ANSYS-Fluent, release 14.5 (ANSYS-Fluent 2012), and the results are compared with experimental data from literature (Brooks *et al.*, 1989; Oerlemans, 2004; Oerlermans, Migliore, 2004), as well as with the predictions of semi-empirical models from (Arbey, Bataille, 1983; Brooks *et al.*, 1989; Paterson *et al.*, 1973).

2. Background information and methodology

The present work applies the two-dimensional URANS simulation methodology augmented with a transitional turbulent model for the aerodynamic simulation and coupled with the Ffowcs Williams and Hawkings for the acoustic prediction. The approach, presented in the next sections, has been chosen for its low-computational burden, showing how it is capable to predict the LBL-VS tonal noise. The methodology is suitable for capturing the tonal noise emission from flow mass displacement and flow interaction with non-permeable surfaces, while it is not suited for predicting noise from turbulence sources, therefore it cannot be extended towards free field problems and jet flows.

2.1. Unsteady Reynolds Averaged Navier-Stokes and transitional turbulence model

The governing Navier-Stokes continuity and momentum equations are averaged over a sufficiently long period in order to lose the turbulent fluctuations but keeping the time dependence of the averaged quantities, according to the classical Unsteady RANS (URANS) formulation (Wilcox, 2010). The mathematical closure of these equations calls for the turbulence model, which can be chosen among a large variety of models available in literature. Among them, one of the model which is most often used for industrial application is the *k-ω* model (Wilcox, 2010), which imposes this closure with two additional equations, i.e. one for the turbulent kinetic energy and one for the dissipation rate respectively, adopted in its Shear Stress Transport (SST) formulation, hence referred as *k-ω* SST turbulence model.

In this article, the transitional extension of the *k-ω* SST turbulence model is used (ANSYS-Fluent 2012; Menter, 1994; Menter *et al.*, 2004). It is based on the coupling of this model with two additional equations: one for the intermittency and one for the transition onset criterion, defined as momentum thickness Reynolds number. The model is based on the Langstry and Menter empirical correlations to cover standard bypass transition as well as flows characterised by low free-stream turbulence. The transport equations for the intermittency γ and for momentum thickness Reynolds number $\mathrm{Re}_{\theta t}$ are given below

$$\frac{\partial(\rho\gamma)}{\partial t} + \frac{\partial(\rho v_j \gamma)}{\partial x_j} = P_{\gamma 1} - E_{\gamma 1} + P_{\gamma 2} - E_{\gamma 2} + \frac{\partial}{\partial x_j}\left[\left(\mu + \frac{\mu_t}{\sigma_\gamma}\right)\frac{\partial \gamma}{\partial x_j}\right], \tag{4}$$

$$\frac{\partial(\rho \mathrm{Re}_{\theta t})}{\partial t} + \frac{\partial(\rho v_j \mathrm{Re}_{\theta t})}{\partial x_j} = P_{\theta t} + \frac{\partial}{\partial x_j} \cdot \left[\sigma_{\theta t}\left(\mu + \mu_t\right)\frac{\partial \mathrm{Re}_{\theta t}}{\partial x_j}\right]. \tag{5}$$

The P and E terms in Eq. (4) can be classified as transitional sources (subscript $\gamma 1$) and destruction/relaminarization sources (subscript $\gamma 2$). The onset transition is controlled by these sources in the form of ANSYS proprietary empirical correlations and these equations are coupled via the $P_{\theta t}$ term in Eq. (5). This model has been explicitly designed to deal with flow characterized by moderate Reynolds number and non-stabilised flow conditions.

2.2. Ffowcs Williams and Hawkings acoustic analogy

The Ffowcs Williams and Hawkings (FW-H) Eq. (6) is an extension of the Lighthill's acoustic analogy (Lighthill, 1952; 1954) that allows to introduce the effects of boundary surfaces by the additional sources, i.e. F and Q, multiplied by the Heaviside function $H(f)$. These additional sources account for the effects of the walls: monopoles, i.e. body thickness effect, and dipoles, i.e. body-flow interaction effect. Indeed the Heaviside function works as a switch to identify emitting surfaces in the domain (i.e. physical or virtual) depending on the position of the boundary nodes in time and space (i.e. $f(\underline{x}, t)$)

$$\frac{1}{a^2}\frac{\partial^2 H(f)p'}{\partial t^2} - \nabla^2[H(f)p'] = \frac{\partial^2}{\partial x_i \partial x_j}[T_{ij}H(f)] + \frac{\partial F_i \delta'(f)}{\partial x_i} + \frac{\partial Q\delta'(f)}{\partial t}. \tag{6}$$

The FW-H equation is solved by means of the free-space Green function, solution of the elementary wave propagation equation forced by time and space impulses. The solution (7) is the sum of the acoustic pressure arising from the different sources: monopoles, dipoles and quadrupoles. It is important to notice that the monopoles and the dipoles are related to surface integrals, while the quadrupoles are volumetric sources. For low Mach number flows, the noise contribution of the quadrupoles is negligible compared to the monopoles and dipoles. Therefore, to reduce the computational burden, the quadrupoles are neglected in this work.

$$\begin{aligned} p'(\underline{x}, t) &= p'_T(\underline{x}, t) + p'_F(\underline{x}, t) + p'_Q(\underline{x}, t) \\ &= \frac{1}{4\pi}\frac{\partial^2}{\partial x_i \partial x_j}\int_{\Omega_1} \frac{T_{ij}H(f)}{|x-\xi|\,|1-M_r|}\,\mathrm{d}\Omega \\ &\quad -\frac{1}{4\pi}\frac{\partial}{\partial x_i}\int_{\Gamma^S} \frac{F_i\delta'(f)}{|x-\xi|\,|1-M_r|}\,\mathrm{d}\Gamma \\ &\quad +\frac{1}{4\pi}\frac{\partial}{\partial t}\int_{\Gamma^S} \frac{Q_i\delta'(f)}{|x-\xi|\,|1-M_r|}\,\mathrm{d}\Gamma. \end{aligned} \tag{7}$$

2.3. Semi-empirical modelling of aerofoil airborne noise

Brooks *et al.* (1989) derived, as result of a vast experimental research campaign on the NACA 0012 aerofoil, a semi-empirical model based on integral boundary layer quantities (later referred as BPM model, from the authors Brooks, Pope and Marcolini) to predict the noise generated by TBL-TE, S-S and LBL-VS mechanisms (see introduction). This model consists of four algebraic equations (8) to predict the TBL-TE, the S-S and the LBL-VS noise spectra, combined to calculate the total SPL according to Eq. (9). In Eq. (8) the δ and δ^* are the boundary layer thickness and the displacement thickness of the boundary layer calculated at the trailing edge of the aerofoil, M is the Mach number, L is the span wise dimension of the aerofoil, r_e is the distance between the trailing edge and the receiver location, and A, B, $K_{1,2}$, $\mathit{\Delta} K_1$ and $G_{1,2,3}$ are the empirical functions based on a set of Strouhal numbers (St), Reynolds number (Re_c) and AoA (α^*). The subscripts p and s refer to pressure and suction side, respectively. Directivity effects are taken into account by means of the correction coefficient D_h (10). This coefficient applies only when the TBL-TE model produces a high frequency noise (up to a threshold AoA). For higher AoAs, corresponding to the near-stall conditions, the turbulent noise contributions are neglected (i.e. $\mathrm{SPL}_{\text{TBL-TE-P}} = \mathrm{SPL}_{\text{TBL-TE-S}} = -\infty$) whereas the S-S contribution remains, being characterised by a low-frequency spectrum. In this case the $\mathrm{SPL}_{\text{S-S}}$ contribution is slightly modified and the correction coefficient for directivity turns into D_l, according to Eq. (11)

$$\begin{cases} \mathrm{SPL}_{\text{TBL-TE-P}} = 10\log\left(\dfrac{\delta_p^* M^5 L D_h}{r_e^2}\right) \\ \qquad + A\left(\dfrac{\mathrm{St}_p}{\mathrm{St}_1}\right) + (K_1 - 3) + \mathit{\Delta} K_1, \\ \mathrm{SPL}_{\text{TBL-TE-S}} = 10\log\left(\dfrac{\delta_s^* M^5 L D_h}{r_e^2}\right) \\ \qquad + A\left(\dfrac{\mathrm{St}_s}{\mathrm{St}_1}\right) + (K_1 - 3), \\ \mathrm{SPL}_{\text{S-S}} = 10\log\left(\dfrac{\delta_s^* M^5 L D_h}{r_e^2}\right) + B\left(\dfrac{\mathrm{St}_s}{\mathrm{St}_2}\right) + K_2, \\ \mathrm{SPL}_{\text{LBL-VS}} = 10\log\left(\dfrac{\delta_p M^5 L D_h}{r_e^2}\right) \\ \qquad + G_1\left(\dfrac{\mathrm{St}'}{\mathrm{St}'_{\text{peak}}}\right) + G_2\left(\dfrac{\mathrm{Re}_c}{\mathrm{Re}_{c,o}}\right) + G_3\left(\alpha^*\right), \end{cases} \tag{8}$$

$$\begin{aligned} \mathrm{SPL}_{\text{TOT}} = 10\log\Big(&10^{\mathrm{SPL}_{\text{TBL-TE-P}}/10} \\ &+10^{\mathrm{SPL}_{\text{TBL-TE-S}}/10} \\ &+ 10^{\mathrm{SPL}_{\text{S-S}}/10} + 10^{\mathrm{SPL}_{\text{LBL-VS}}/10}\Big), \end{aligned} \tag{9}$$

$$D_h = \frac{2\sin\left(\mathit{\Theta}_e/2\right)\sin^2\mathit{\Phi}_e}{\left(1 + M\cos\mathit{\Theta}_e\right)\left[1 + (M - M_c)\cos\mathit{\Theta}_e\right]^2}, \tag{10}$$

$$\begin{aligned} \mathrm{SPL}_{\text{S-S}} &= 10\log\left(\frac{\delta_s^* M^5 L D_l}{r_e^2}\right) + A'\left(\frac{\mathrm{St}_s}{\mathrm{St}_2}\right) + K_2, \\ D_l &= \frac{\sin^2\mathit{\Theta}_e\sin^2\mathit{\Phi}_e}{\left(1 + M\cos\mathit{\Theta}_e\right)^4}. \end{aligned} \tag{11}$$

The BPM model has been implemented by the authors in an in-house developed MATLAB® (Mathworks Inc., 2011) tool and interfaced with ANSYS-Fluent, to compute the boundary layer thickness and displacement thickness input data. This interface is a critical issue since a reliable detection of the boundary layer border from CFD velocity profiles is the key for computing the boundary layer integral quantities. The BPM model and its CFD interface have been developed for general-purposes three-dimensional applications, and validated on a number of different geometries (i.e. NACA 0012, NACA 4412, DU96 (De Gennaro, Kuehnelt, 2012a), 6-bladed axial fan (De Gennaro, Kuehnelt, 2012a; 2012b)) and mesh topologies (i.e. tetrahedral, hexahedral, polyhedral mesh volume cell). These studies have confirmed the robustness of the boundary layer extraction and border-detection procedure, enabling the BPM model to be used for a number of different applications and geometries. In this work, this model is adopted to benchmark the FW-H results, especially for receivers' locations and conditions where no experimental data is available.

2.4. LBL-VS experimental datasets

Two experimental datasets are considered to benchmark the simulation results presented in this paper: the dataset provided by Brooks *et al.* (1989) and the dataset provided by Oerlemans and Migliore (Oerlemans, 2004; Oerlemans, Migliore, 2004). In the first case the NACA 0012 aerofoil, with a chord of 22 cm and a sharp trailing edge, is tested in the low-turbulence core of a free jet located in an anechoic chamber. The measurements are performed at free-stream flow velocities ranging from 30 to 70 m/s and AoA ranging from 0 to 15.6°. The acoustic measurements are performed with microphones located as sketched in Fig. 2a, at a distance of 1.22 m (5.5 chords lengths), and with a visual angle of −30° (M1), 0° (M2) and +30° (M3) with respect to the trailing edge. The Power Spectral Density Level (PSDL) of the acoustic pressure at the microphones locations is given in one-third octave bands from 0.2 to 10 kHz, assuming a reference pressure equal to $20 \cdot 10^{-6}$ Pa.

The second experimental dataset is derived from the experimental campaign conducted in the open-circuit NLR's Small Anechoic Wind Tunnel KAT by Oerlemans and Migliore (Oerlemans, 2004; Oerlemans, Migliore, 2004). The NACA 0012 aerofoil model, with a chord length of 22 cm and a sharp trailing edge, was tested for the same aerodynamic conditions tested by Brooks *et al.* (1989). The microphone array (Fig. 2b) consists of 48 microphones mounted in an open grid designed for maximum side-lobe suppression at frequencies between 1 and 20 kHz. The averaged PSDL of the acoustic pressure is provided from 0.8 to 10 kHz in one-third octave bands.

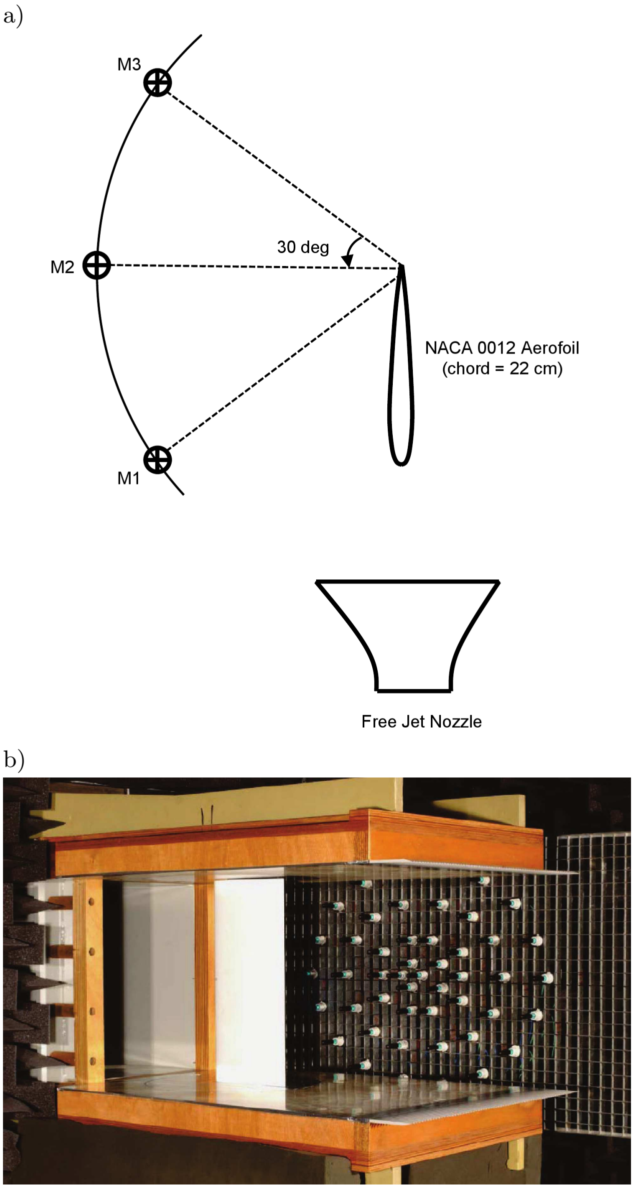

Fig. 2. Sketch of the NASA experimental setup (Brooks *et al.*, 1989), (a) NRL's KAT wind tunnel test chamber instrumented with the microphones star array (b) (Oerlemans, Migliore, 2004; Oerlemans, 2004).

2.5. Test-matrix and numerical setup of the simulations

Based on the two experimental data sets described in Subsec. 2.4, the authors have defined the test-matrix reported in Table 1. The test conditions are chosen in order to pick the LBL-VS as the predominant noise generation mechanism, occurring for the NACA 0012 aerofoil for an AoA of 4 and 5°, at moderate Reynolds numbers (i.e. approximately between $0.5 \cdot 10^6$ and $1 \cdot 10^6$). Therefore, given the aerofoil chord equal to 0.22 m, the Mach number is set to range from 0.07 to 0.22, resulting in a Reynolds number ranging from $0.39 \cdot 10^6$ to $1.09 \cdot 10^6$.

Table 1. Aerodynamic coefficients and range of the fluctuations (mesh dependency analysis).

Run ID	Angle of attack [°]	Flow speed [m/s]	Reynolds number	Mach number
Run-1	4	40	$0.62 \cdot 10^6$	0.11
Run-2	5	40	$0.62 \cdot 10^6$	0.11
Run-3	4	25	$0.39 \cdot 10^6$	0.07
Run-4	4	55	$0.85 \cdot 10^6$	0.15
Run-5	4	70	$1.09 \cdot 10^6$	0.20
Run-6	5	70	$1.09 \cdot 10^6$	0.20

The flow solution for the test conditions of Table 1 is computed with the numerical approach described in Subsec. 2.1 (i.e. URANS coupled with the transitional k-ω SST turbulence model) on a computational grid of 110,000 rectangular cells (later referred as Mesh-1). Mesh-1 is designed to always provide more than 20 cells per wavelength (at 10 kHz) and never less than 20 cells in boundary layer in the orthogonal-to-surface direction, for all test conditions reported in Table 1. The wall y^+ results to be always below one on the aerofoil surface and the far-field boundary condition is set at 20 chords of distance from the aerofoil. Six probes are placed on the aerofoil surface (three on the pressure side and three on the suction side) at the 95%, 97.5% and 99% of the chord length. Additionally eleven rakes are set on the aerofoil pressure and suction surfaces, (from 10% to 90% of the chord length, equally spaced, plus one at 95% and one at 99%), in the orthogonal-to-surface direction. Each rake extends for 5% of the chord length, with the lower node placed in the first cell of the computational grid and the upper node placed above the upper border of the boundary layer. Two hundreds flow velocity points are extracted along the rake, capturing at least one value per each cell of the computational grid. Then the extracted velocity profile is processed, applying the boundary layer edge detection procedure described in Subsec. 2.3. This consists of placing the upper cut-off of the boundary at a location where the velocity profile becomes nearly vertical with respect to the local normal-to-surface direction. This is assumed by looking at the slope of a linear regression of a sliding window containing 4 different consequent values of the total pressure profile, and placing the cut-off when this exhibits an angular deviation to the local vertical direction below 10°. The probes and the rakes record the hydrodynamic pressure fluctuations, the mean pressure and the mean velocity in different locations of the boundary layer.

A picture of the computational grid at the leading and at the trailing edge of the aerofoil is provided in Fig. 3, where the boundary layer refinement is visible. An additional computational grid is generated for carrying out the mesh dependency analysis, later referred to as Mesh-2, derived by dividing each mesh cell of Mesh-1 into four cells, thus resulting in 440,000 cells.

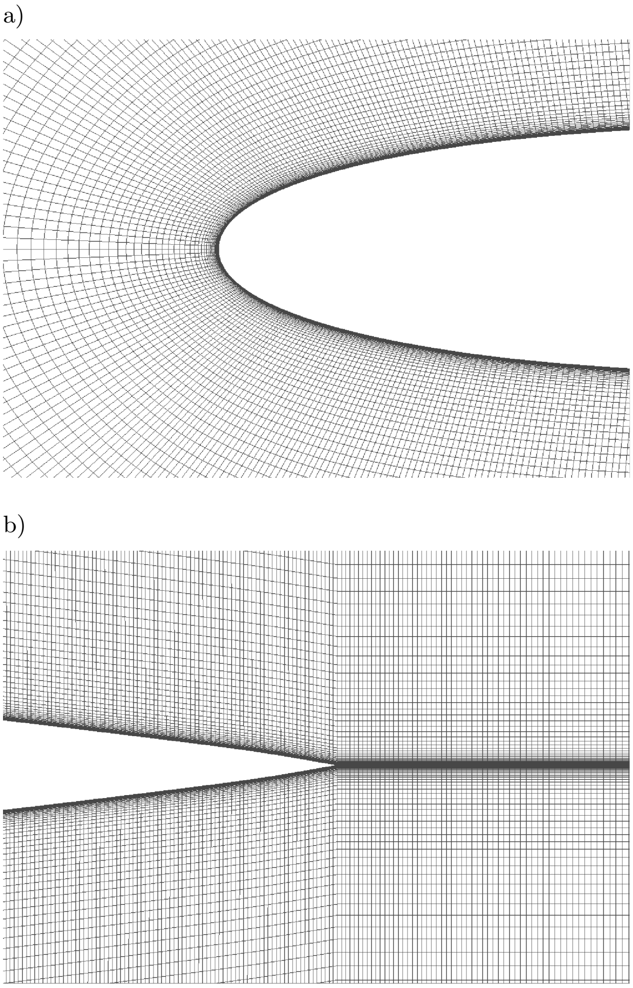

Fig. 3. Computational grid details for Mesh-1: a) leading edge, b) trailing edge.

The pressure-based solver is used for the URANS solution, with the SIMPLE scheme for the pressure-velocity coupling, the Standard scheme for the pressure and the QUICK scheme for the discretization of the momentum, energy and turbulence equations (ANSYS-Fluent, 2012). The boundary conditions are set as “wall” for the aerofoil, “velocity-inlet” for the inlet and “pressure-outlet” for the outlet, set at standard atmospheric conditions. Inlet turbulence was set at 0.05%, while under-relaxation factors were set at 0.5. The steady RANS solution is used to initialise the unsteady solver, which runs until a fully developed periodic flow solution is calculated (periodicity is calculated by monitoring aerodynamics forces and pressure on the aerofoil surface). Then the acoustic data acquisition campaign is carried out with 20,000 time-steps with a simulation time-step size of 10^{-5} s. The acoustic sampling is set every second time-step for a total sampling time of 0.2 s and 10^4 acoustic samples, thus providing a spectral frequency resolution of approximately 10 Hz and a maximum resolved frequency of approximately 25 kHz. The time series of the acoustic pressure at the receivers' locations M1, M2 and M3 are computed with the two-dimensional formulation of the FW-H acoustic analogy. Such implementation needs the source correlation length as further input parameter of the analogy, as per (ANSYS-Fluent, 2012). This parameter represents the dimension of the coherent vortical structures in the spanwise direction of the aerofoil, which is infinite in a two-dimensional problem. Clearly infinite cannot be set, hence, in order not to incur into spurious errors coming from the FW-H numerical implementation, the source correlation length is suggested to be set significantly larger (ideally one order of magnitude) than the chord of the aerofoil. In this work, the source correlation length has been set equal to 10 m; however, this length does not influence the predicted acoustic level, since the level is scaled down to the physical spanwise extension of the aerofoil, according to the Eq. (13) described below (i.e. $\text{Span}_{\text{Corr}}$).

The sound-pressure signals are processed with an in-house developed MATLAB® tool to compute the narrowband/one-third octave band PSDL spectra of the acoustic pressure. The PSDL is calculated by applying the Discrete Fourier transform (DFT) of the acoustic pressure signal via the Fast Fourier Transform (FFT) routines implemented in MATLAB® (Mathworks Inc., 2011). The formula used for the narrowband PSDL computation is reported in Eq. (12), where $x[i]$ is the discrete pressure time signal, F is the discrete Fourier transform, N is the number of samples, and $20 \cdot 10^{-6}$ [Pa] is the reference pressure

$$\text{PSDL} = 10 \log_{10} \left(\frac{2 \left| \frac{F(x[i])}{N} \right|^2}{\left(20 \cdot 10^{-6}\right)^2} \right). \tag{12}$$

The PSDL is also calculated in one-third octave band by integrating the spectral content (i.e. $F(x[i])$) over the third octave bands and divided by the band widths (i.e. averaged one-third octave band plot). In order to compare the results from the different experimental datasets, the simulation results and the experimental data from Oerlemans and Migliore (Oerlemans, 2004; Oerlermans, Migliore, 2004) are scaled both to the experimental conditions set by Brooks *et al.* (1989): span size of the model equal to 0.45 m and microphones distance from the aerofoil equal to 1.22 m. The scaling formula used is provided by Bies and Hansen (2009) and provides a correction to apply to PSDL to account for the span size dimension (i.e. first term in Eq. (13)), and for the distance of the microphones from the trailing edge (i.e. second term in Eq. (13)). Note that in Eq. (13) the subscripts 0 and 1 refer to an initial and final condition respectively, while the quantities S and r_e are the dimensional semi-span of the aerofoil and the distance of the microphones from the trailing edge expressed in m. Additionally, the application of the spanwise correction $\text{Span}_{\text{Corr}}$ to the PSDL calculated with a spanwise source correlation length of 10 m is equivalent to assume that the vortical structures that generate the noise are perfectly coherent across the full spanwise dimension of the tested aerofoil and this is consistent with the two-dimensional nature of the LBL-VS noise generation mechanisms.

$$\begin{aligned}\text{PSDL}_{\text{Corr}} &= \text{Span}_{\text{Corr}} + \text{Dist}_{\text{Corr}} \\ &= 10 \log_{10} \left[\frac{\tan^{-1}\left(\frac{S_0}{r_{e,o}}\right) + \frac{\sin(2\cdot\tan^{-1}(S_0/r_{e,o}))}{2}}{\tan^{-1}\left(\frac{S_1}{r_{e,o}}\right) + \frac{\sin(2\cdot\tan^{-1}(S_1/r_{e,o}))}{2}} \right] \\ &\quad + 20 \log_{10} \left(\frac{r_{e,1}}{r_{e,0}} \right).\end{aligned} \tag{13}$$

3. Results

The flow computed for all the test conditions reported in Table 1 exhibits pressure fluctuations on the aerofoil surface. These fluctuations are visible on the aerodynamic coefficients (i.e. lift and drag coefficients), on the pressure coefficient and on the velocity and vorticity contours. The instabilities appear confined in the boundary layer region close to the aerofoil surface, moving in the direction of the flow stream. This phenomenon appears on the suction side only, establishing at approximately one third of the chord length, lasting up to the till the transition-to-turbulence coordinate. Downstream this point the instabilities disappear, while the pressure side of the aerofoil is entirely characterised by laminar flow field without flow instabilities, except some minor fluctuations at the trailing edge.

In order to present the aerodynamic results, both instantaneous and time-averaged quantities are reported. Later on the text refers as "instantaneous" to the results derived from a snapshot of the solution at the last time step of the simulation (i.e. after the acoustic sampling period of 0.2 s), whereas it refers as "time-averaged" to the results derived as averaged quantities over the entire acoustic sampling period.

Table 2 reports the time-averaged lift and drag coefficients for the flow conditions of Table 1 (i.e. C_l and C_d, respectively), normalised with respect to the asymptotic dynamic pressure multiplied by the aerofoil chord length. The values in parenthesis are the half peak-to-peak amplitude of the fluctuations of the aerodynamic coefficients. The drag coefficient is reported in drag-counts (i.e. $C_d \cdot 10^4$). It can be noticed that the fluctuations are more prominent on the drag coefficient than on the lift coefficient, being the latter less sensitive to the instabilities in the boundary layer.

Table 2. Time-averaged aerodynamic coefficients and amplitude of the fluctuations.

Run ID	AoA [°]	Reynolds number	Lift coefficient and amplitude $C_{l,\text{ time-averaged}}$ (amplitude)	Drag coefficient and amplitude $C_{d,\text{ time-averaged}}$ (amplitude) $\cdot 10^4$
Run-1	4	$0.62 \cdot 10^6$	0.46 (±0.04)	71 (±30)
Run-2	5	$0.62 \cdot 10^6$	0.61 (±0.02)	82 (±24)
Run-3	4	$0.39 \cdot 10^6$	0.47 (±0.06)	96 (±45)
Run-4	4	$0.85 \cdot 10^6$	0.44 (±0.02)	60 (±10)
Run-5	4	$1.09 \cdot 10^6$	0.45 (±0.01)	55 (±5)
Run-6	5	$1.09 \cdot 10^6$	0.55 (±0.01)	63 (±5)

Figure 4 reports the pressure coefficient results (instantaneous and time-averaged) on the aerofoil surface, for the test conditions of Run-1 and Run-2 (Table 1). Both instantaneous solutions exhibit large fluctuations of the pressure coefficient, while the time-averaged solutions are smooth, resembling the steady solution. This suggests that the pressure fluctuations can be seen as transient phenomena superimposed to a stable mean flow solution. The wobble, visible in the mean solution, appears to be located in the position where the fluctuations originate, signalling the instabilities' trigger.

Figures 5 and 6 report the time-averaged velocity and pressure profiles extracted from the orthogonal-to-surface rakes placed on the aerofoil surface (see Subsec. 2.5). For brevity only the rakes located at 30%, 60% and 99% of the chord length are reported (suction and pressure side), for the flow conditions of Run-1 and Run-2 (Table 1). Black squares on the y-axis indicate the boundary layer upper cut-off, according to the border detection procedure described in Subsec. 2.5. This y-coordinate is used as upper integration limit to compute the displacement thickness of the boundary layer, according to Eq. (14), (Schlichting, 1979). The time-averaged velocity and density profiles (i.e. $v(y)$ and $\rho(y)$) extracted at 99% of the chord length are used to compute δ^*, for the pressure and suction side, reported in Table 3

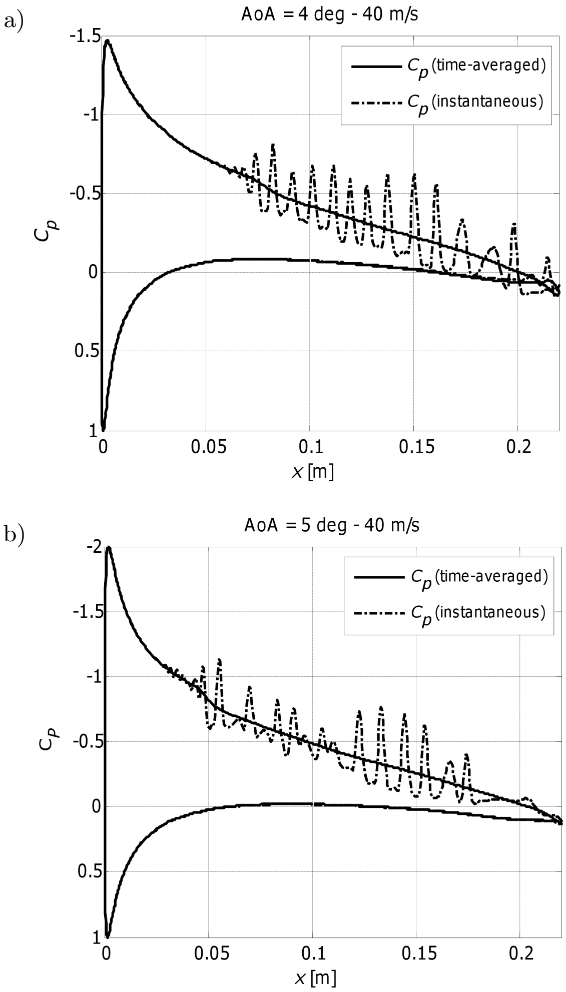

Fig. 4. Pressure coefficient on the aerofoil surface, time averaged versus instantaneous: a) Run-1, b) Run-2.

$$\delta^* = \int\limits_0^\delta \left(1 - \frac{v(y)\rho(y)}{v_o\rho_o}\right) \mathrm{d}y. \tag{14}$$

Table 3. Displacement thickness (δ^*) at 99% of the chord length in [m], pressure and suction side. Transition-to-turbulence coordinates pressure and suction side.

Run ID	δ^* – suction side, at 99% of the chord (time-averaged) [m] $\cdot 10^2$	δ^* – pressure side, at 99% of the chord (time-averaged) [m] $\cdot 10^2$	Transition [x_{tr}/chord], suction side	Transition [x_{tr}/chord], pressure side
Run-1	0.0012	0.00094	0.80	no transition
Run-2	0.0012	0.0012	0.68	
Run-3	0.0016	0.0015	0.95	
Run-4	0.0011	0.00067	0.79	
Run-5	0.00093	0.00060	0.76	
Run-6	0.0011	0.00062	0.72	

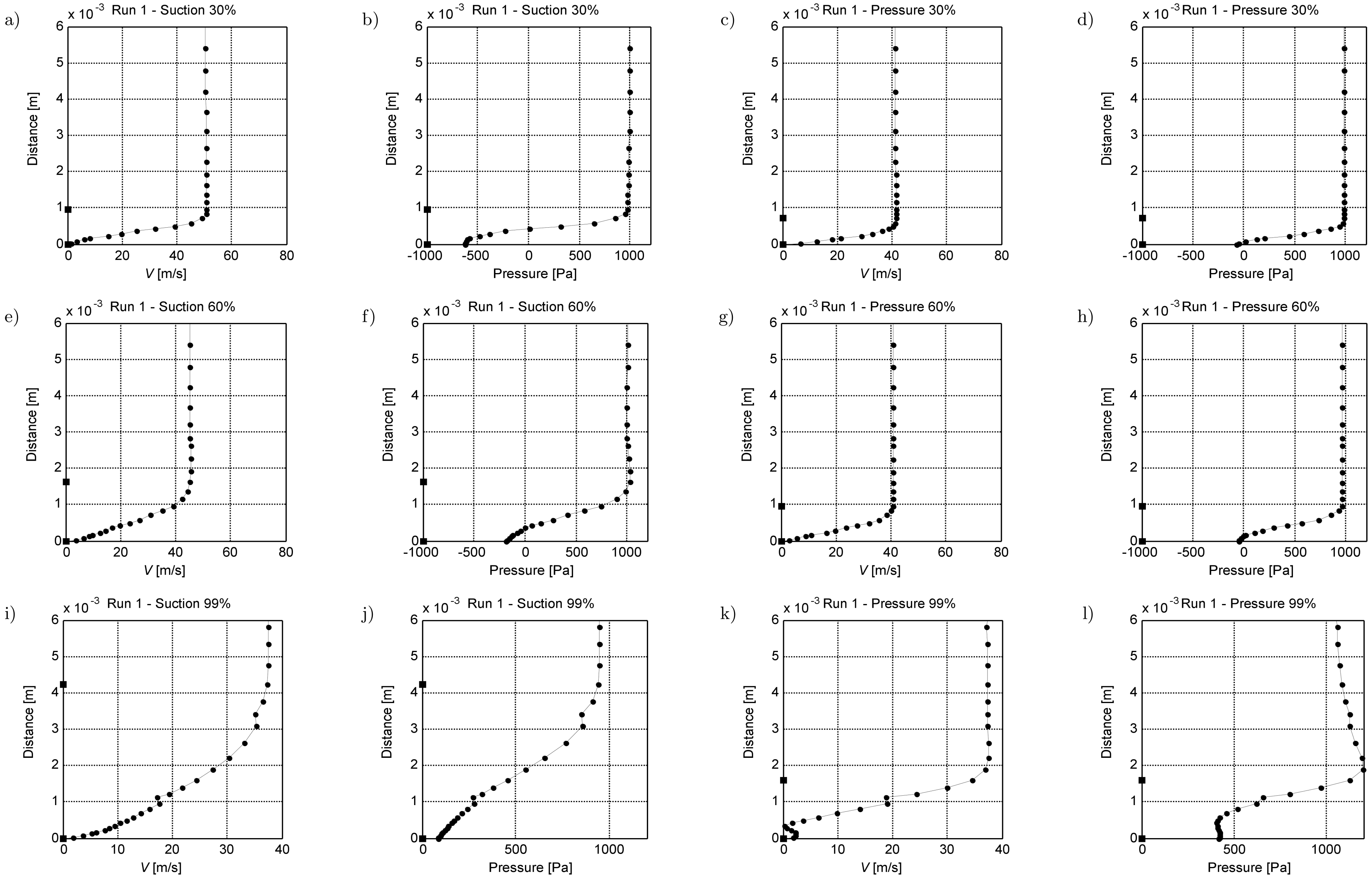

Fig. 5. Velocity [m/s] and pressure [Pa] profiles extracted from the orthogonal-to-surface rakes placed on the aerofoil surface, at the 30% ((a)–(d)), 60% ((e)–(h)) and 99% ((i)–(l)) of the chord length (suction and pressure side). Run-1 of Table 1. The black square on the y-axis indicates the boundary layer upper cut-off, according to the border detection procedure described in Subsec. 2.5.

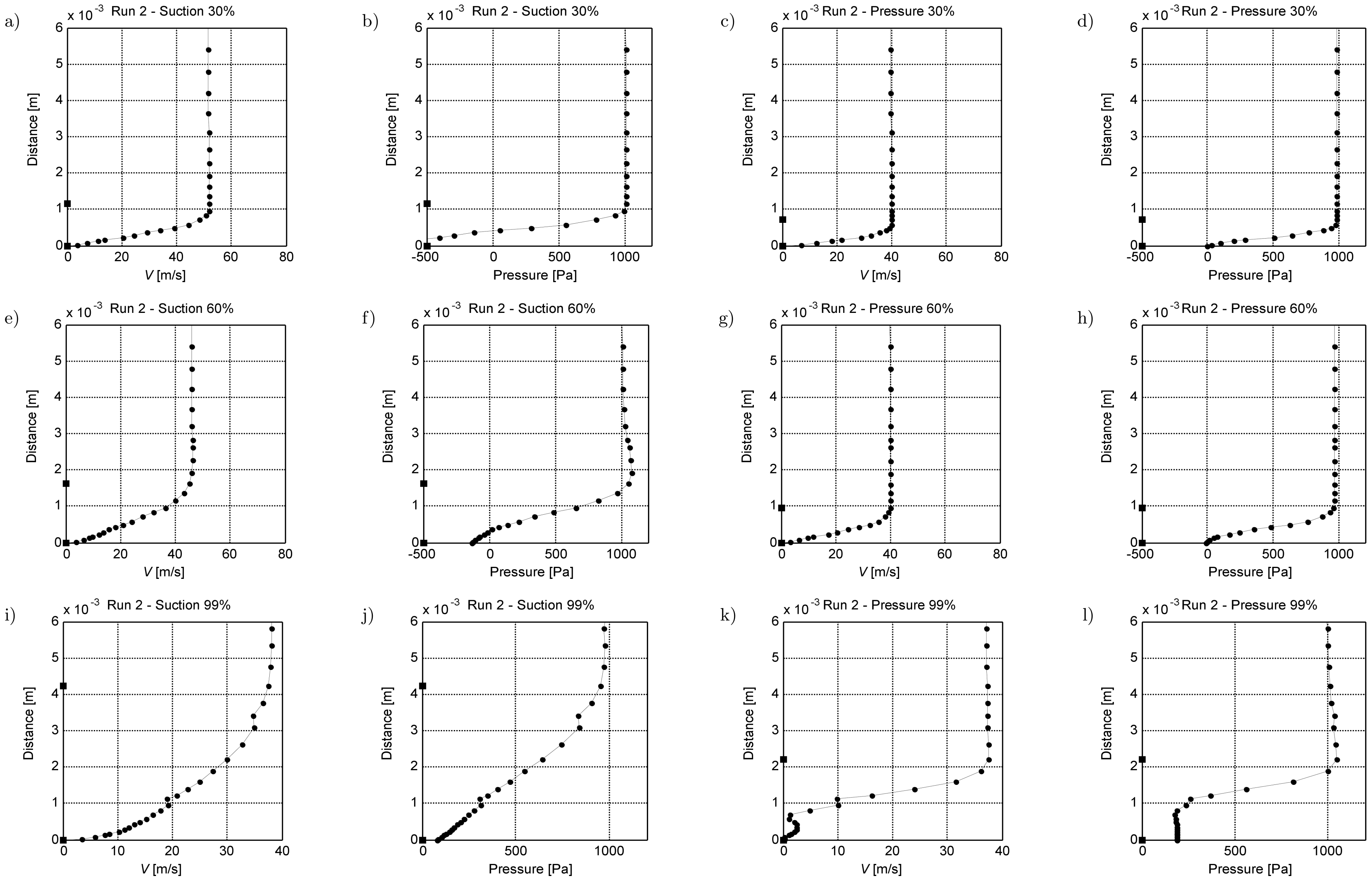

Fig. 6. Velocity [m/s] and pressure [Pa] profiles extracted from the orthogonal-to-surface rakes placed on the aerofoil surface, at the 30% ((a)–(d)), 60% ((e)–(h)) and 99% ((i)–(l)) of the chord length (suction and pressure side). Run-2 of Table 1 The black square on the y-axis indicates the boundary layer upper cut-off, according to the border detection procedure described in Subsec. 2.5.

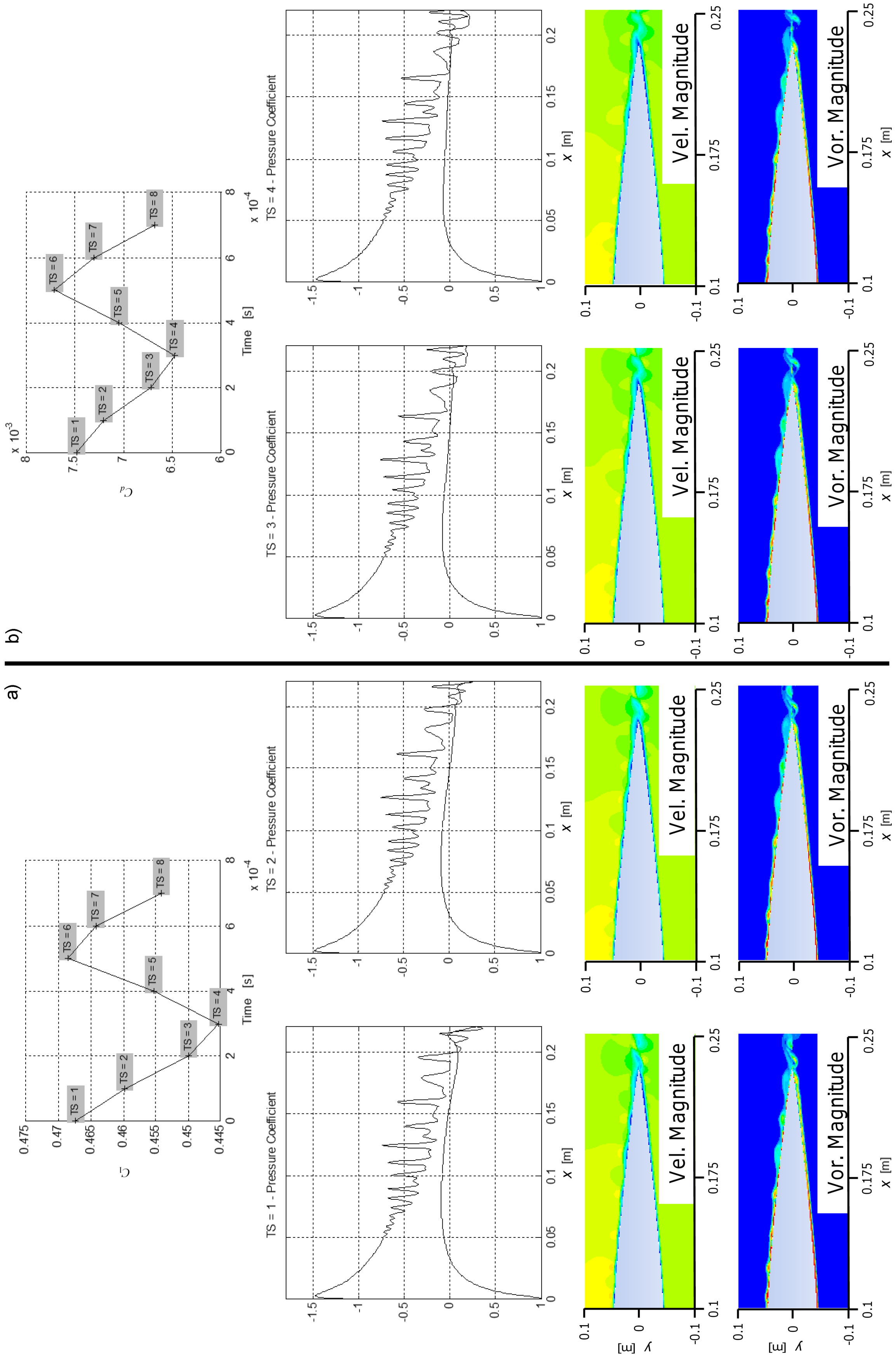
a)
b)
C_l
C_d
x 10^{-3}
Time [s]
x 10^{-4}
TS = 1
TS = 2
TS = 3
TS = 4
TS = 5
TS = 6
TS = 7
TS = 8
TS = 1 - Pressure Coefficient
TS = 2 - Pressure Coefficient
TS = 3 - Pressure Coefficient
TS = 4 - Pressure Coefficient
x [m]
y [m]
Vel. Magnitude
Vor. Magnitude

[Fig. 7]

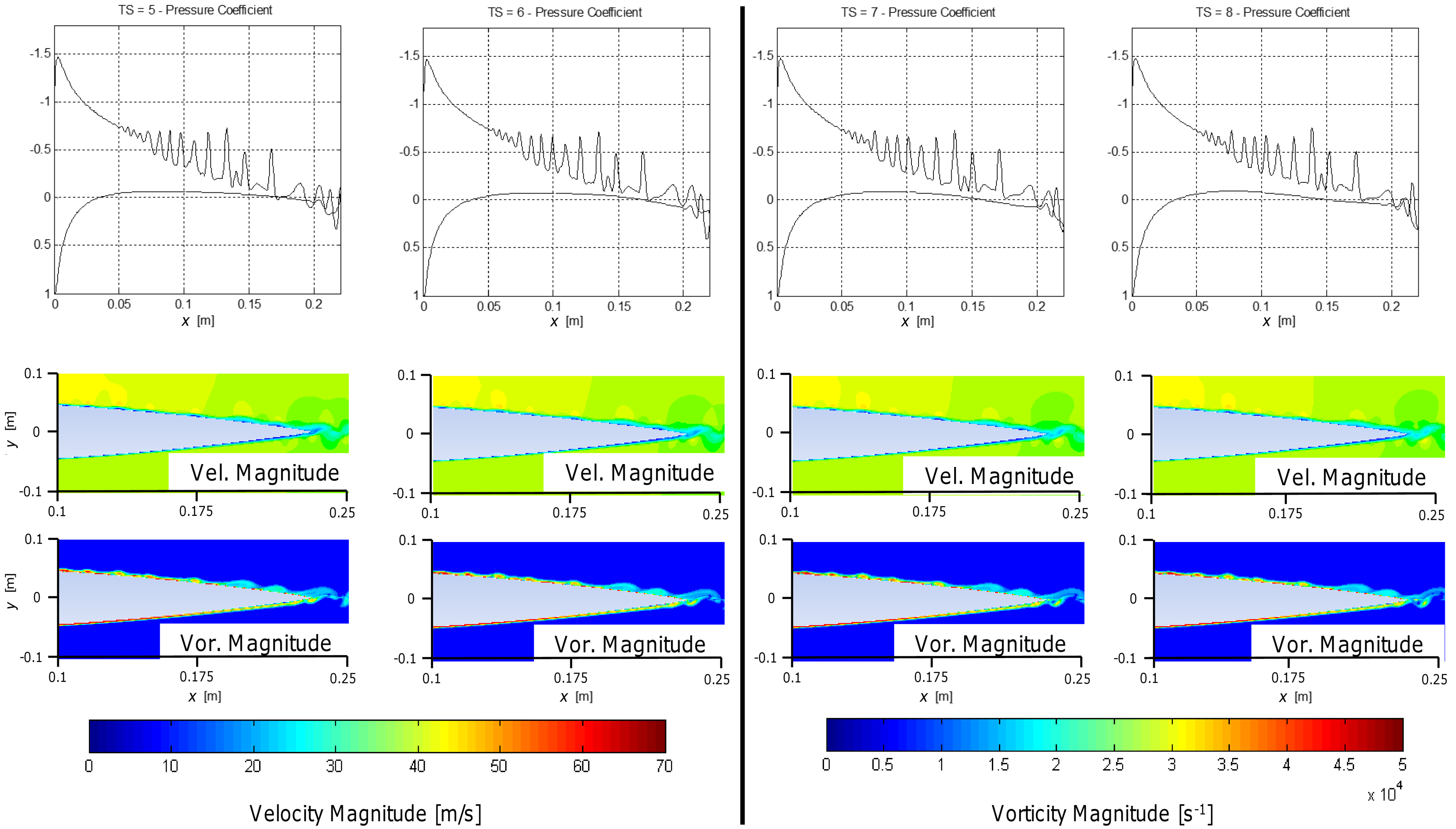

Fig. 7. Flow solution visualization for Run-1. Eight solution samples are reported over a period of $7 \cdot 10^{-4}$ s (i.e. one frame each 10^{-4} s or each 10 simulation time-steps). The oscillation of the aerodynamic coefficient (i.e. C_l and C_d), the pressure coefficient over the aerofoil and the velocity and vorticity magnitude contours are reported.

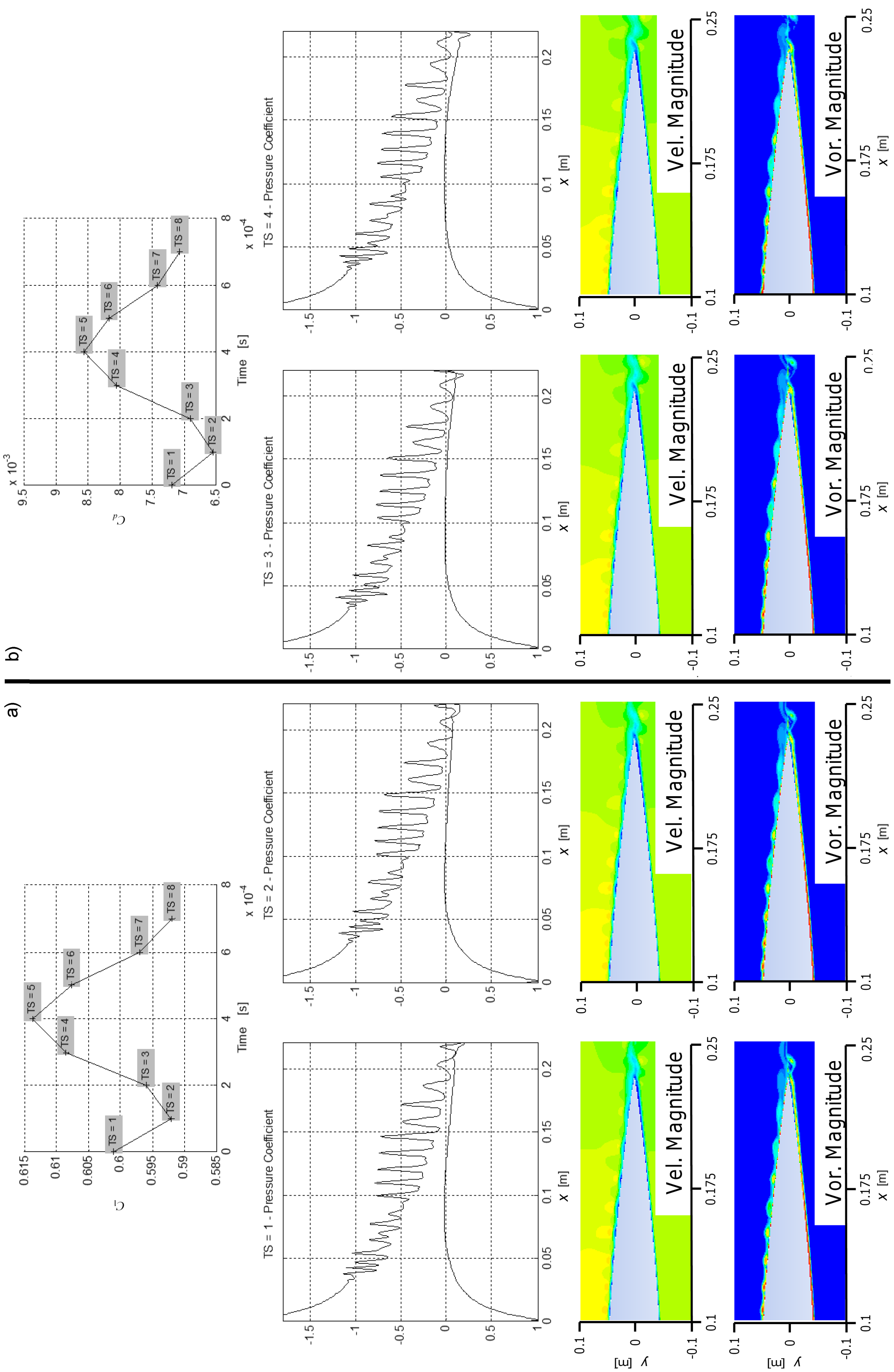
a)
b)
C_l
C_d
0.615
0.61
0.605
0.6
0.595
0.59
0.585
x 10^-3
9.5
9
8.5
8
7.5
7
6.5
0
2
4
6
8
x 10^-4
Time [s]
TS = 1
TS = 2
TS = 3
TS = 4
TS = 5
TS = 6
TS = 7
TS = 8
TS = 1 - Pressure Coefficient
TS = 2 - Pressure Coefficient
TS = 3 - Pressure Coefficient
TS = 4 - Pressure Coefficient
-1.5
-1
-0.5
0
0.5
1
0.05
0.1
0.15
0.2
x [m]
Vel. Magnitude
Vor. Magnitude
y [m]
0.1
0
-0.1
0.175
0.25

[Fig. 8]

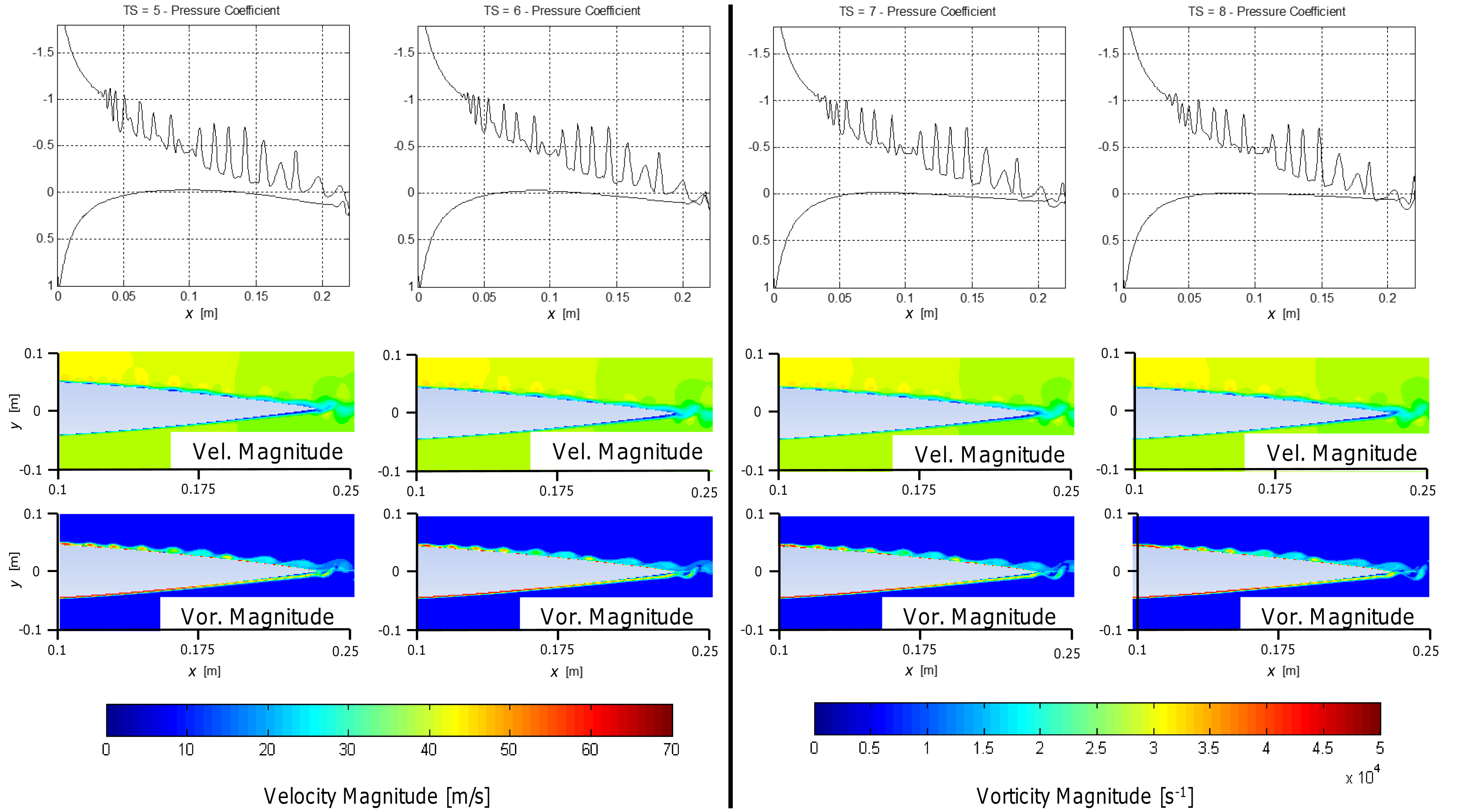

Fig. 8. Flow solution visualization for Run-2. Eight solution samples are reported over a period of $7 \cdot 10^{-4}$ s (i.e. one frame each 10^{-4} s or each 10 simulation time-steps). The oscillation of the aerodynamic coefficients (i.e. C_l and C_d), the pressure coefficient over the aerofoil and the velocity and vorticity magnitude contours are reported.

Table 3 reports the transition-to-turbulence coordinate (suction side), assumed as the chord coordinate where the computed flow intermittency γ first becomes equal to one in the boundary layer. This coordinate oscillates according to the upstream boundary layer instabilities and the coordinates reported in Table 3 represent the earliest transition-to-turbulence point detected for every test conditions.

The results show that the flow solution is characterised by a late transition-to-turbulence, exhibiting a widely extended laminar region of the boundary layer in the suction side. Moreover, a kink in the velocity and pressure profile for the extractions at 99% of the chord is visible in Figs. 5 and 6. This kink is due to the presence of recirculating flow at the trailing edge, as presented in the next pictures.

Figures 7 and 8 report the flow solution, for the test conditions of Run-1 and Run-2 respectively. The fluctuations are represented by choosing 8 time-steps (from TS = 1 to TS = 8) over a sampling time of $7 \cdot 10^{-4}$ s (i.e. time-step size equal to 10^{-4} s, each time step reported is taken every 10 computational time-steps). Figures (a) and (b) show the periodic fluctuation of the aerodynamic forces coefficients (i.e. lift and drag respectively), while the eight frames below represent the aerodynamic pressure coefficient on the aerofoil surface, the velocity and the vorticity magnitude contours for the eight time-steps chosen. It is noteworthy that each fluctuation of the aerodynamic forces coefficients goes from approximately TS = 1 to TS = 6 for Run-1, while it goes approximately from TS = 1 to TS = 7 for Run-2. The laminar instabilities are well visible on the pressure coefficient curves, and the downstream flow oscillations can be traced by following the pressure expansion peaks on the suction surface through subsequent frames. The effects of these instabilities are visible by analysing the velocity and vorticity contours, which show a large instability region developed over the suction side of the aerofoil and an oscillating wake released at the trailing edge.

Figures 9 and 11 report the PSDL of the acoustic pressure in narrowband spectrum in both logarithmic and linear scale (FW-H results), whereas Figs. 10 and 12 report the PSDL of the acoustic pressure in one-third octave band spectrum. The spectra are provided for the microphone locations M1, M2 and M3 (see Subsec. 2.4) and in a frequency range from 0.5 to 10 kHz. As far as the one-third octave band plots are concerned, the FW-H simulation results are compared with the experimental data from Brooks *et al.* (1989), with the experimental results from Oerlemans and Migliore (Oerlemans, 2004; Oerlermans, Migliore, 2004), as well as with the predictions of the BPM semi-empirical model for the microphone location M2. On the other hand, not being available the experimental data for M1 and M3, the FW-H simulation results for these two microphone locations are only compared with the predictions from the BPM

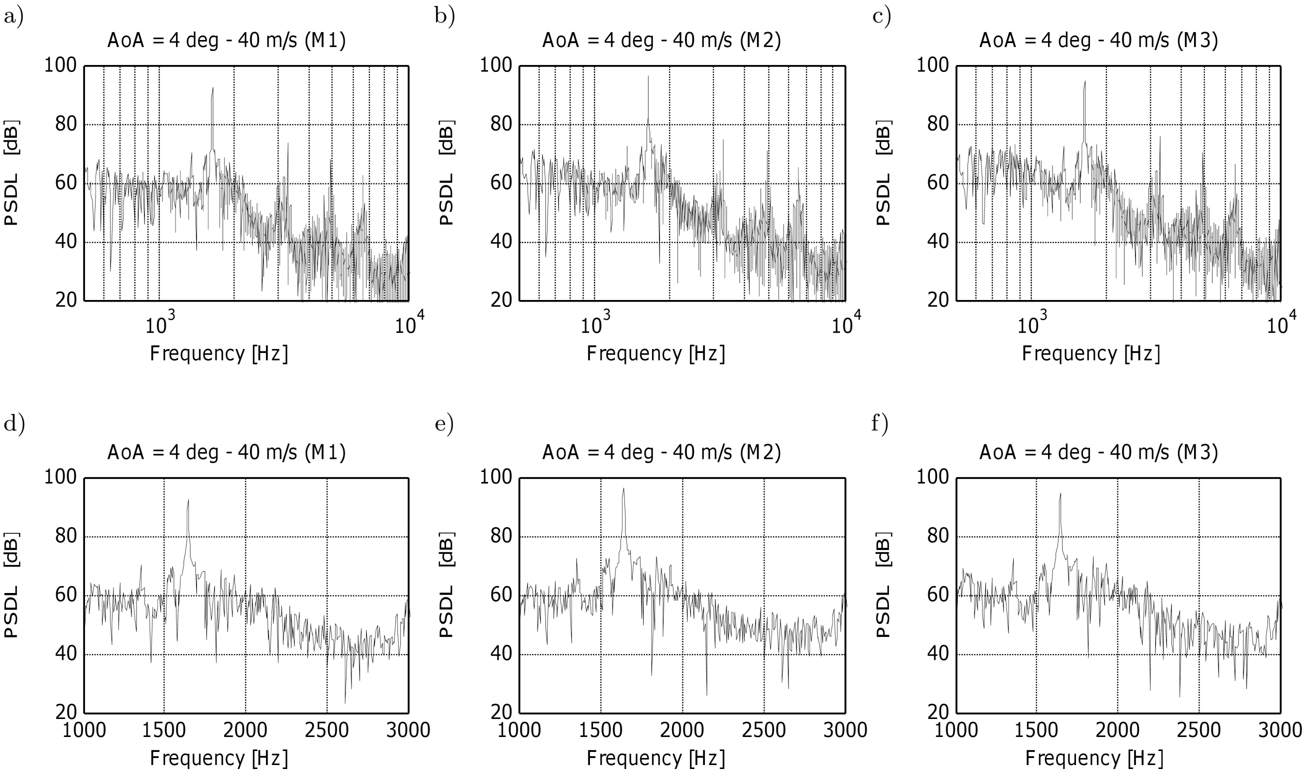

Fig. 9. Run-1, PSDL of the acoustic pressure in narrowband spectrum calculated with FW-H. Comparison for different microphone locations: a)–c) in logarithmic scale between 0.5 and 10 kHz, d)–f) in linear scale between 1 and 3 kHz.

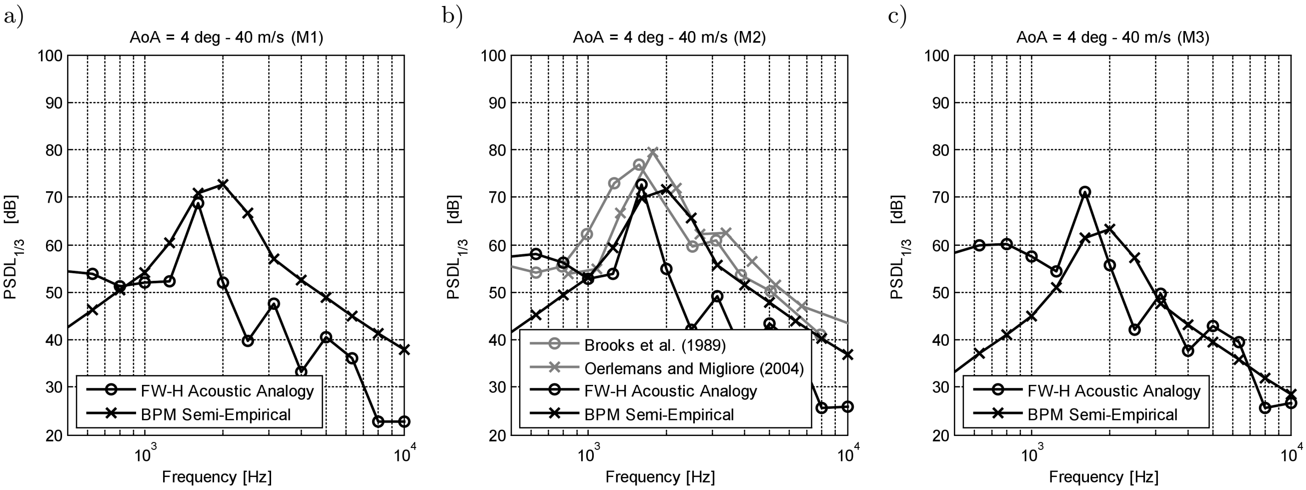

Fig. 10. Run-1, PSDL of the acoustic pressure in one-third octave band. FW-H, BPM and experimental comparison for M1 (a), M2 (b) and M3 (c).

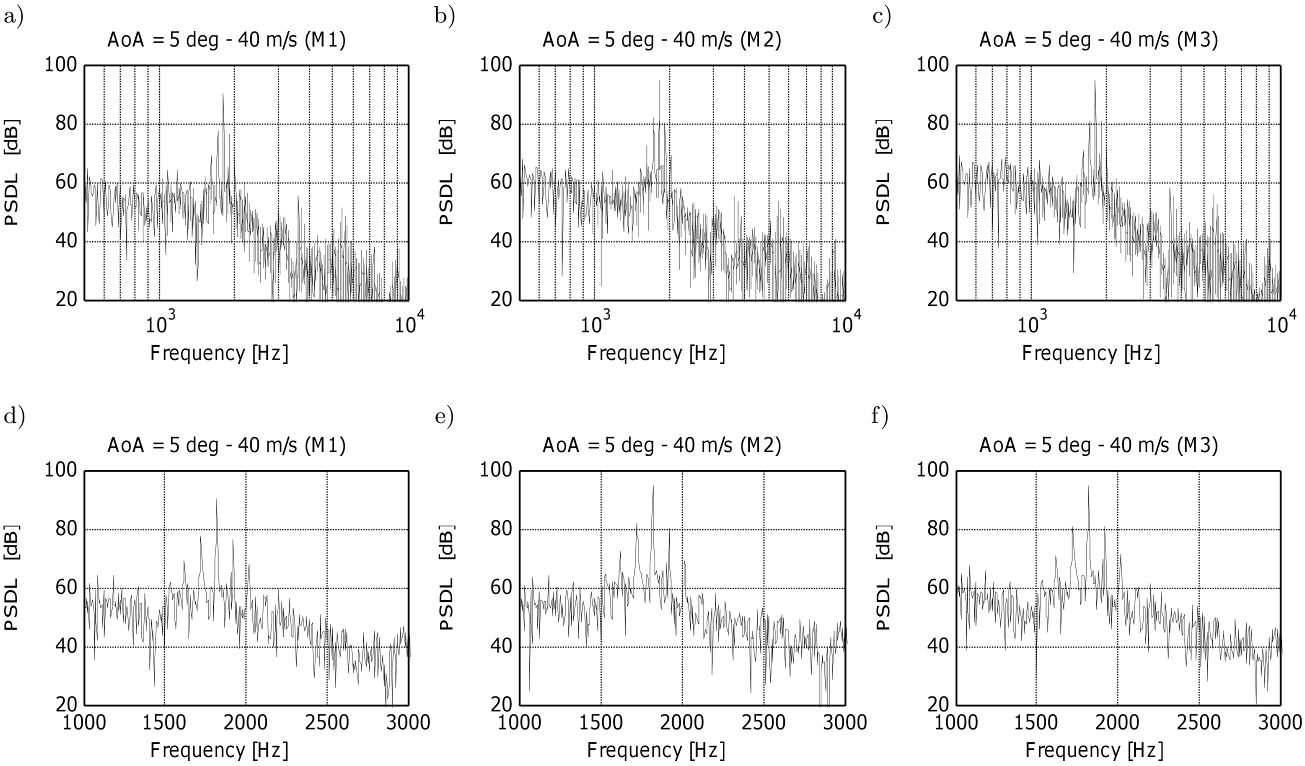

Fig. 11. Run-2, PSDL of the acoustic pressure in narrowband spectrum calculated with FW-H. Comparison for different microphone locations: a)–c) in logarithmic scale between 0.5 and 10 kHz, d)–f) in linear scale between 1 and 3 kHz.

semi-empirical model. The FW-H results, compared with the experimental measurements of Brooks *et al.* (1989), show that the simulations are capable of predicting the main tone frequency location and magnitude for both angles of attack (about 1.6 kHz for AoA of 4° and 1.8 kHz for AoA of 5°) with higher accuracy than the BPM semi-empirical model. The broadband part of the spectrum (i.e. the off-tone regions), which cannot be predicted by URANS simulations due to the turbulence modelling and which is generated by the TBL-TE mechanism, is not present in the FW-H results, hence explaining the differences up to 30 dB with the experimental data and the semi-empirical model predictions. However, given the tonal nature of the acoustic spectra, as per experimental datasets and BPM predictions, and given the 15–20 dB off-tone drop of the PSDL observed at the 1 kHz and 3 kHz in the experimental data, we can conclude that the weight of the broadband components is negligible in the one-third octave band computation. Therefore, the compu-

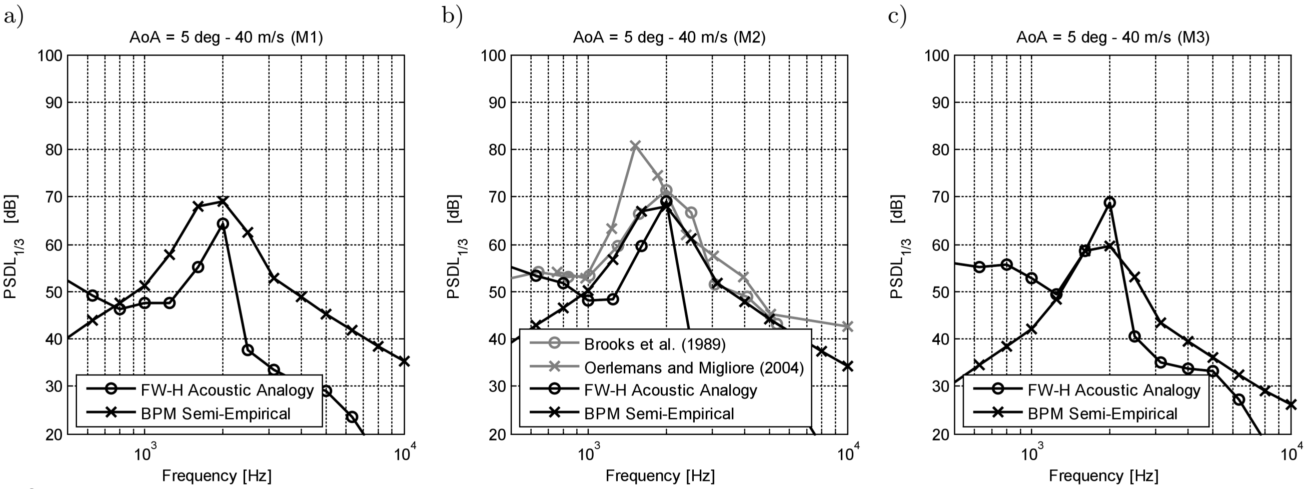

Fig. 12. Run-2, PSDL of the acoustic pressure in one-third octave band. FW-H, BPM and experimental comparison for M1 (a), M2 (b) and M3 (c).

tation of the PSDL of the peak is not affected by the fact that the FW-H computation misses the broadband noise spectral content, and its level can be considered accurate.

The narrowband spectra show instead that the single peak visible in one-third octave band spectra is made of a main tone, located approximately at 1.6 kHz for Run-1 and 1.8 kHz for Run-2 (i.e. Reynolds number equal to $0.62 \cdot 10^6$), plus a number multiple tones, well-visible in the linear scale close-up. Additional tones, located in correspondence of the multiples of the main tone frequency, are also visible. The tonal structure derived is in agreement with that described in literature by (Arbey, Bataille, 1983; Paterson *et al.*, 1973), confirming the physical representation of the phenomenon as composed by one main tone combined with several secondary tones according to a multi-tonal structure.

A frequency analysis is presented for the hydrodynamic pressure signals at the trailing edge. Figures 13 and 14 report the frequency spectrum of the hydrodynamic pressure signals (i.e. PSDL_H), computed

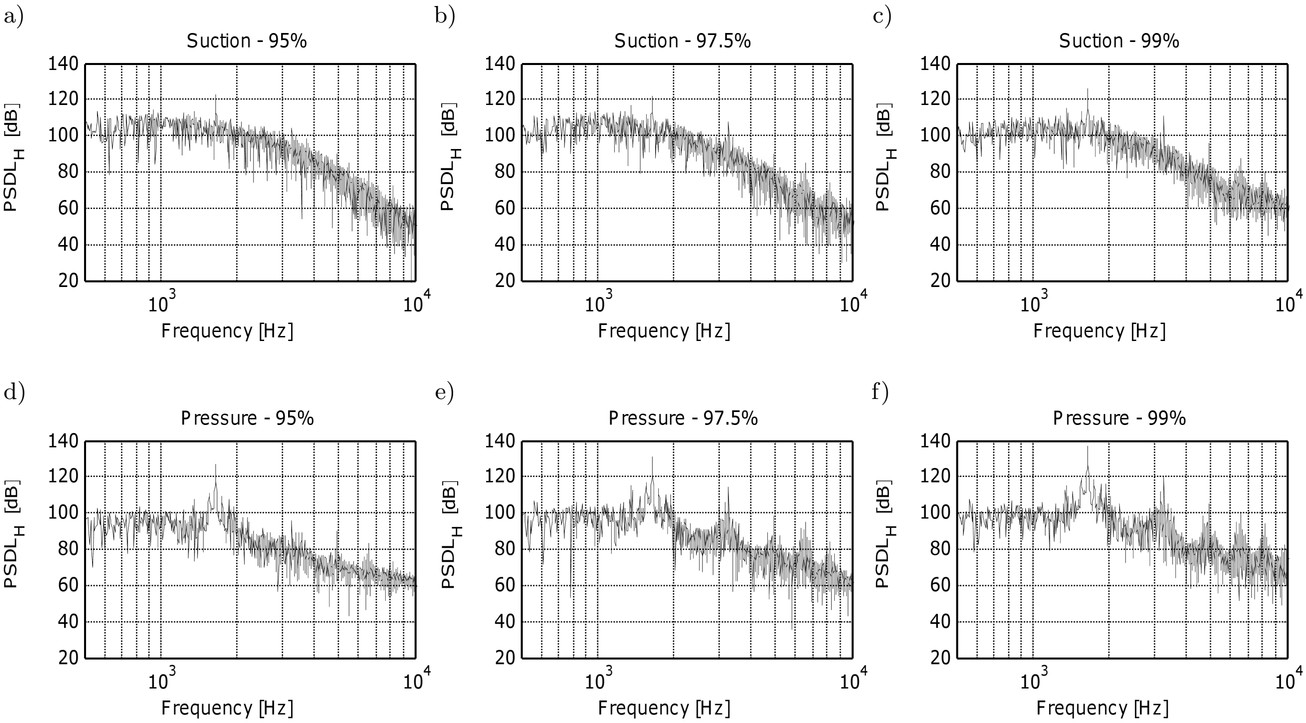

Fig. 13. Run-1, PSDL of the hydrodinamic pressure (i.e. PSDLH) in narrowband spectrum in logarithmic scale between 0.5 and 10 kHz, measured on the aerofoil surface at 95%, 97.5% and 99% of the chord length: a)–c) suction side, d)–f) pressure side.

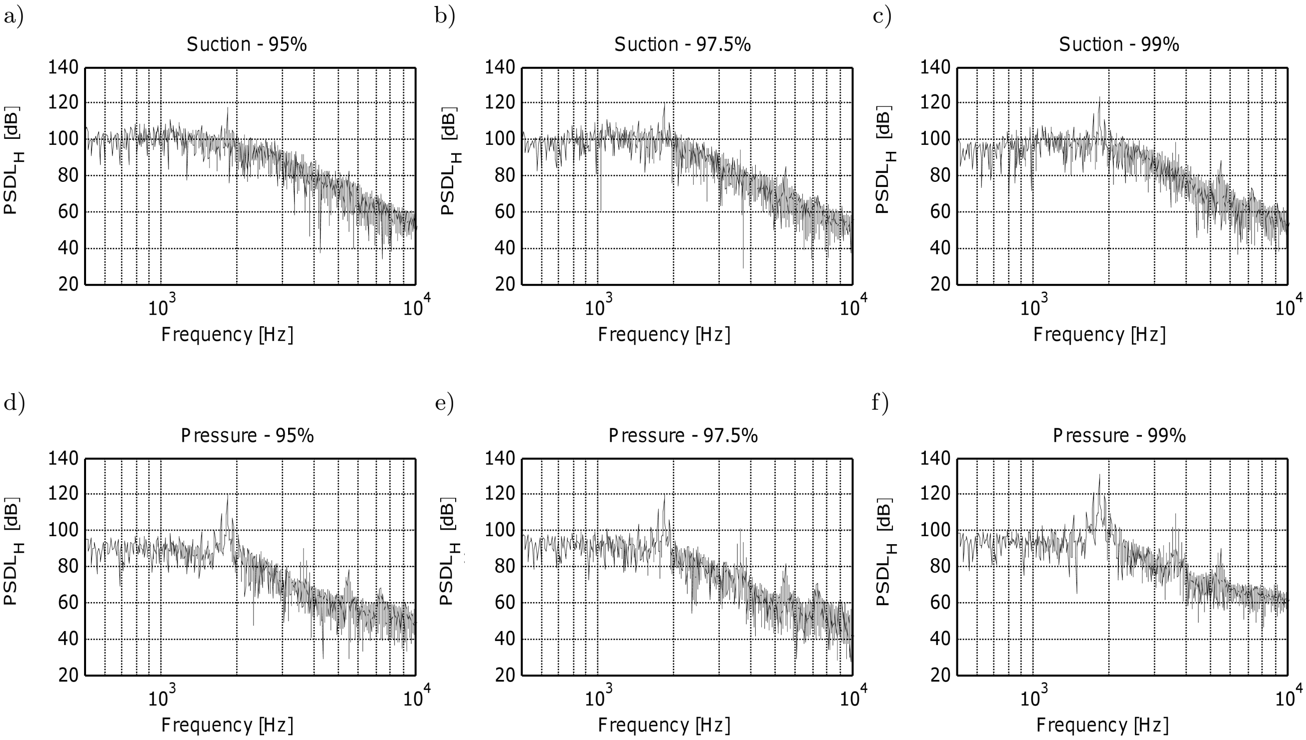

Fig. 14. Run-2, PSDL of the hydrodynamic pressure (i.e. PSDLH) in narrowband spectrum in logarithmic scale between 0.5 and 10 kHz, measured on the aerofoil surface at 95%, 97.5% and 99% of the chord length: a)–c) suction side, d)–f) pressure side.

according to Eq. (12), for test conditions of Run-1 and Run-2 respectively. The pressure probes at 95%, 97.5% and 99% of the chord length on the suction side (from (a) to (c)), and on the pressure side (from (d) to (f)) are considered, and the processed hydrodynamic pressure time signals have been acquired over the complete acoustic sampling period (i.e. 0.2 s). As in the case of the acoustic pressure, these spectra exhibit a main tone frequency on both pressure and suction side, whose frequency is in line with that of the acoustic pressure main tone. Secondary harmonics are also visible, especially at the 99% probe location and especially at the pressure side. However, these secondary tones in the hydrodynamic pressure spectra are less visible than in the acoustic pressure spectra, being partially masked by the turbulence of the boundary layer that generates broadband noise.

Figure 15 reports the narrowband spectra of the FW-H simulation results in logarithmic scale for the microphones locations M1, M2 and M3 and in a range of frequencies from 0.5 to 10 kHz for the test conditions from Run-3 to Run-6. These results show that no tones appear for Run-3 (i.e. Reynolds number equal to $0.39 \cdot 10^6$), while they appear for Run-4, 5 and 6 (i.e. Reynolds number equal to $0.85 \cdot 10^6$ and $1.09 \cdot 10^6$). The higher the Reynolds number, the higher the frequency of the main tone becomes, increasing to 2.4 kHz at Reynolds number equal to $0.85 \cdot 10^6$ and 3.4 kHz at $1.09 \cdot 10^6$. Figure 16 depicts the comparison between the dependency of the main tone frequency on the flow speed predicted by the FW-H acoustic analogy and the results of the semi-empirical models presented in the Sec. 1, i.e. the Paterson *et al.* formula (1), and the Arbey and Bataille formula (2). The frequency of the main tone is located in correspondence with the maximum PSDL of the acoustic spectrum. This comparison is performed for all the flow conditions reported in Table 1, except for Run-3 where no major tones are predicted. The FW-H predictions of the main tone frequency are in agreement with Paterson's formula (1) for all the investigated conditions, whereas a disagreement of approximately 500 Hz is found with the formula from Arbey and Bataille, Eq. (2), at 4° and for the flow speeds of 55 and 70 m/s. Beyond this, the result substantially confirms the ladder-like structure of the main tone, suggesting the validity of the experimental observations conducted so far.

In order to validate the results presented, a mesh-dependency analysis is reported, carried out for the test condition of Run-1. Table 4 presents the comparison of the lift and drag coefficients computed with the Mesh-1 and Mesh-2 (see Subsec. 2.5). As per Table 2, these coefficients are normalised with respect to the asymptotic dynamic pressure multiplied by the aerofoil chord length, while the values in parenthesis are the half peak-to-peak amplitude of the fluctuations.

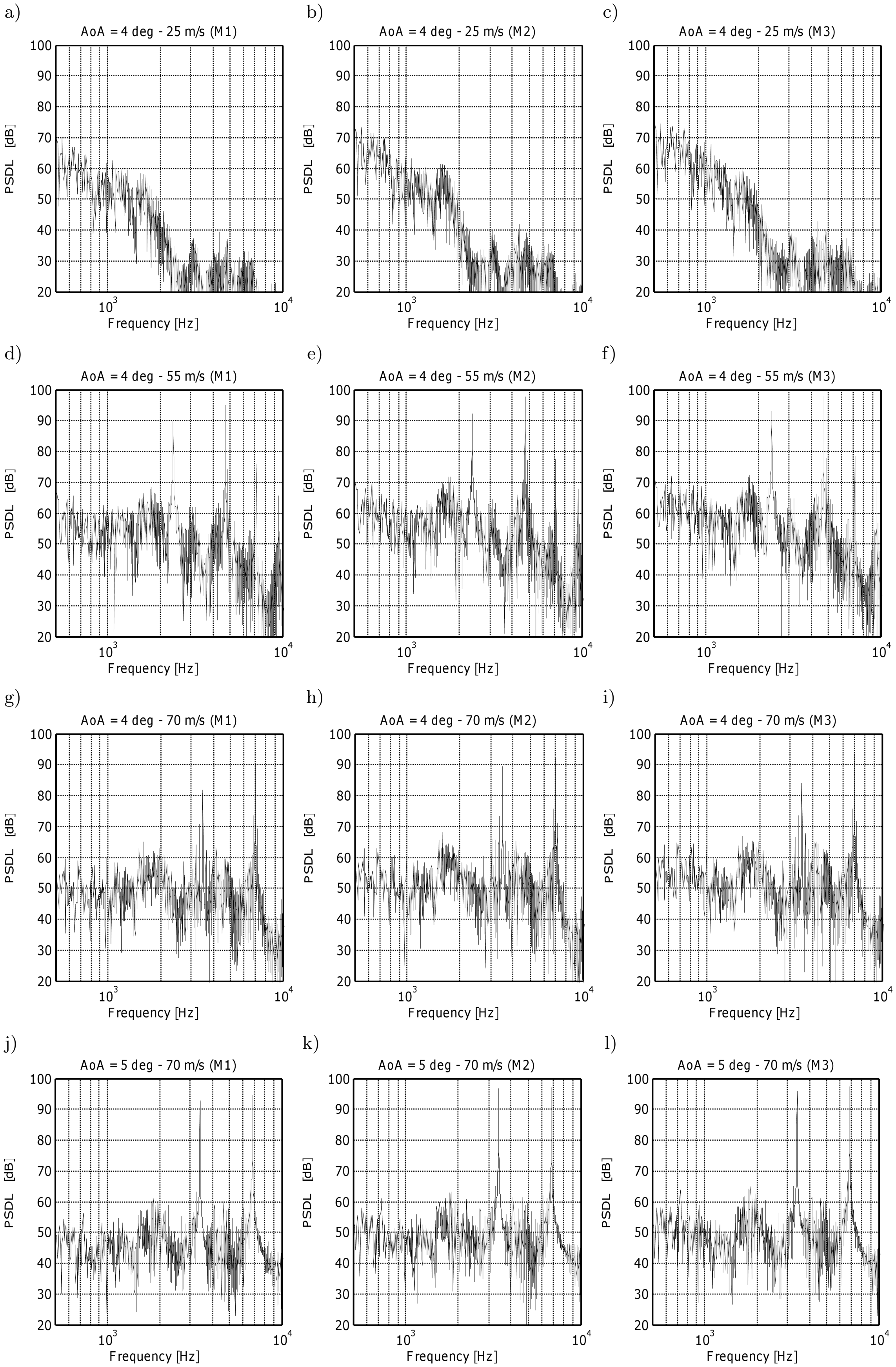

Fig. 15. PSDL of the acoustic pressure in narrowband spectrum calculated with FW-H. Comparison for different microphone locations: a)–c) Run-3, d)–f) Run-4, g)–i) Run-5, j)–l) Run-6.

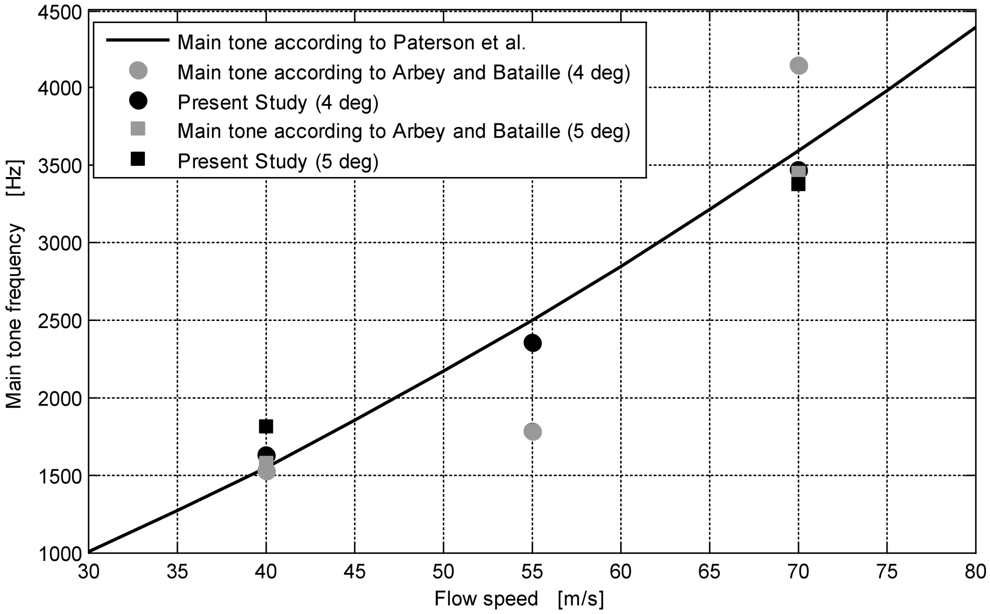

Fig. 16. Comparison of main tone peak frequency predicted by FW-H (black circles and squares, present study) with Paterson *et al.* formula (continuous black line) and Arbey and Bataille formula (grey circles and squares). The data at 40 m/s correspond to the test conditions of Run-1 and Run-2, the data at 55 m/s to Run-4 and the data at 70 m/s to Run-5 and Run-6 (referred to Table 1). Run-3 (i.e. flow speed of 25 m/s) is not reported, not exhibiting a main tone.

Table 4. Aerodynamics coefficients and range of the fluctuations (mesh dependency analysis.

Run and Mesh ID	Lift coefficient and range $C_{l,\text{ time-averaged}}$ (range)	Drag coefficient and range $C_{d,\text{ time-averaged}}$ (range) $\cdot 10^4$
Run-1 – Mesh-1	0.46 (±0.04)	71 (±30)
Run-1 – Mesh-2	0.47 (±0.03)	76 (±21)

Moreover, Fig. 17 reports the comparison of the pressure coefficient (Fig. 17a), and the PSDL spectrum for M2 (Fig. 17b), for the two computational grids considered. These results show that no major differences occur by changing the number of the mesh cells of a factor 4, neither in the aerodynamic flow field nor in the acoustic spectrum shape, confirming the validity of the results of Mesh-1.

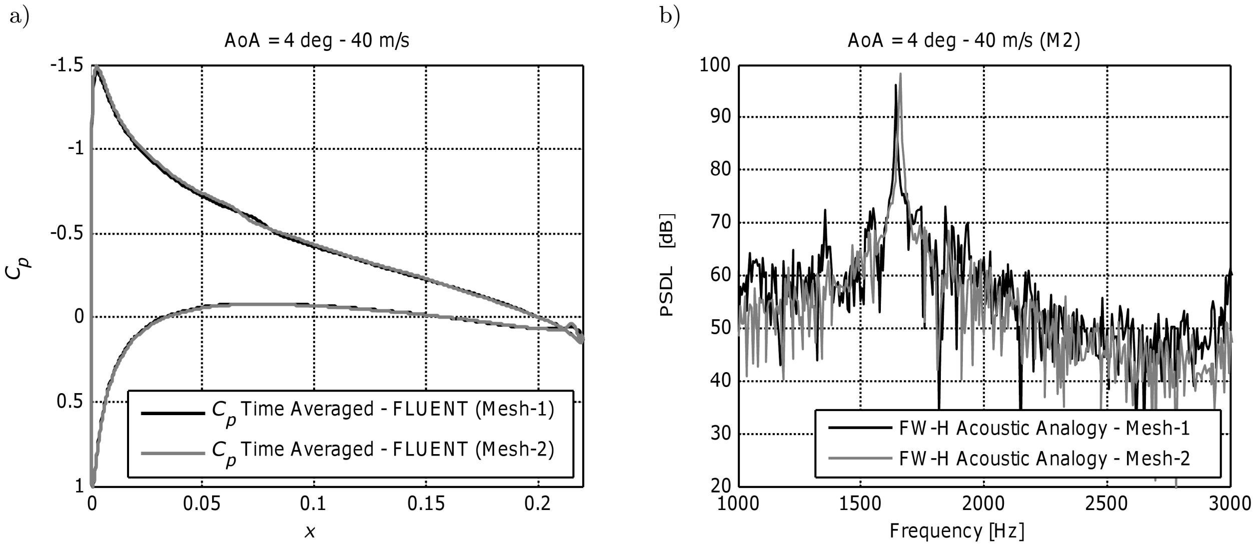

Fig. 17. Mesh dependency analysis, sensitivity of aerodynamic and acoustic results to Mesh-1 (i.e. $110 \cdot 10^3$ cells) and Mesh-2 (i.e. $440 \cdot 10^3$ cells). Comparison of the time averaged pressure coefficient (a) and PSDL of the acoustic pressure calculated with FW-H in linear scale from 1 kHz and 3 kHz (b) for the microphone location M2.

4. Conclusions

This paper presents the results of numerical experiments for evaluating the capability of capturing the tonal airborne noise by using an advanced, yet low computationally demanding, numerical approach. The adopted test case consists of a NACA 0012 aerofoil, in a range of moderate Reynolds number from $0.39 \cdot 10^6$ to $1.09 \cdot 10^6$ and angles of attack from 4° to 5°. Six flow conditions have been investigated, by means of two-dimensional compressible simulations carried out with an URANS approach coupled with the k-ω SST transitional turbulence model, whereas the acoustic propagation is performed with the Ffowcs Williams and Hawkings acoustic analogy.

The simulations show that the flow at Reynolds number equal to $0.62 \cdot 10^6$ is characterised by laminar instabilities which develops in the boundary layer region over the suction surface of the aerofoil, resulting in fluctuations of its aerodynamic coefficients (i.e. lift and drag coefficients), surface pressure coefficient and velocity and vorticity contours. The instantaneous versus time-averaged pressure coefficients suggest that these fluctuations are transient phenomena superimposed to the stable mean flow solution.

The PSDL spectra of the acoustic pressure are computed for three microphone locations in a frequency range from 0.5 to 10 kHz. The results show a main tone located approximately at 1.6–1.8 kHz for a Reynolds number equal to $0.62 \cdot 10^6$, increasing to 2.4 kHz at Reynolds number equal to $0.85 \cdot 10^6$ and 3.4 kHz at $1.09 \cdot 10^6$. The results are in general agreement with the data from semi-empirical models and experiments from literature, with secondary tones visible both in the acoustic pressure spectrum as well as in the hydrodynamic pressure spectrum in the boundary layer. The simulation results confirm the ladder-like structure of the main tone proposed by Paterson *et al.* and its dependency on the flow speed.

Furthermore, the results also confirm the multitonal nature of the acoustic spectra suggested by Arbey and Bataille and well visible in the narrowband acoustic spectra.

Additionally, the results demonstrate that this noise generation mechanisms can be simulated with a relatively low-computational demanding URANS approach given its two-dimensional nature. This is also reflected in the assumption made on the source correlation length, assumed equal to 10 meters for the FW-H calculations and then scaled down to the physical length of the aerofoil. This, in fact, implies that the vortex shedding structures generated by the LBL-VS mechanism are perfectly two-dimensional, thus not considering deformation and distortion which would reduce the source correlation length itself. In this respect, a three-dimensional LES/DNS can be beneficial; however, they would require significant computational resources, not necessarily justified by an improvement on the quality of the noise predictions.

The presented methodology is intended to be applicable only for the LBL-VS noise generation mechanism, and therefore, cannot be extended to other noise generations mechanisms, such as TBL-TE/S-S noise for aerofoils or jet noise for free stream jets, where the phenomenon is driven by three-dimensional turbulent structures. Future developments of the present work can include new testing conditions, as per recent contributions from (Arcoundoulis *et al.*, 2013) and (Pröbsting *et al.*, 2015).

References

1. ANSYS-Fluent 14.5 Theory Guide, ANSYS Inc., 2012.
2. Arbey H., Bataille J. (1983), *Noise generated by aerofoil profiles placed in a uniform laminar flow*, Journal of Fluid Mechanics, **134**, 33–47.
3. Arcondoulis E.J.G., Doolan C.J., Brooks L.A., Zander A.C. (2011), *Aerofoil trailing edge noise source location at low to moderate Reynolds number*, AIAA 2011–2785, 17th AIAA/CEAS Aeroacoustic Conference, Portland, Oregon.
4. Arcondoulis E.J.G., Doolan C.J., Zander A.C., Brooks L.A. (2013), *An experimental investigation of airfoil tonal noise*, Proceedings of Acoustics, Victor Harbor, Australia.
5. Bies D.A., Hansen C.H. (2009), *Engineering noise control*, 4th Ed., Taylor & Francis Spon Press.
6. Brentner K.S., Farassat F. (1998), *An analytical comparison of the acoustic analogy and Kirchhoff formulations for moving surfaces*, AIAA Journal, **36**, 8, 1379–1386, doi: 10.2514/2.558.
7. Brooks T.F., Pope D., Marcolini A. (1989), *Aerofoil self-noise and prediction*, NASA Reference Publication 1218.
8. Chong T.P., Joseph P.F., Kingan M.J. (2013), *An investigation of airfoil tonal noise at different Reynolds numbers and angles of attack*, Applied Acoustics, **74**, 1, 38–48.
9. Curle N. (1953), *The mechanics of edge tones*, Proceedings of the Royal Society A, **216**, 1126, 412–424, doi: 10.1098/rspa.1953.0030.
10. De Gennaro M., Kuehnelt H. (2011), *Semi-empirical modelling of broadband noise for aerofoils*, AIP Conference Series, **1389**, 1498–1502.
11. De Gennaro M., Kuehnelt H. (2012a), *Broadband noise modelling and prediction for axial Fans*, Proceedings of the International Conference Fan Noise, Technology and Numerical Methods, Paris, France.
12. De Gennaro M., Kuehnelt H. (2012b), *CPU efficient flow-acoustic design for axial fans*, SAE Technical Paper 2012-01-1564.
13. De Gennaro M., Zanon A., Kuehnelt H., Giannattasio P. (2012), *Zonal large eddy simulation for numerical prediction of the acoustic performance of an*

axial fan, 6th European Congress on Computational Methods in Applied Sciences and Engineering, Vienna, Austria.

14. Desquesnes M., Terracol M., Sagaut P. (2007), *Numerical investigation of the tone noise mechanism over laminar aerofoils*, Joural of Fluid Mechanics, **591**, 155–182, doi: 10.1017/S0022112007007896.
15. Ewert R., Schröder W. (2003), *Acoustic perturbation equations based on flow decomposition via source filtering*, Journal of Computational Physics, **188**, 365–398.
16. Ewert R., Schröder W. (2004), *On the simulation of trailing edge noise with a hybrid LES/APE method*, Journal of Sound and Vibration, **270**, 509–524.
17. Ffowcs-Williams E., Hawkings D.L. (1969), *Sound Generation by Turbulence and Surfaces in Arbitrary Motion*, Philosophical Transactions of the Royal Society of London. Series A, Mathematical and Physical Sciences, **264**, 1151, 321–342.
18. Fuglsang P., Madsen H.A. (1996), *Implementation and verification of an aeroacoustic noise prediction model for wind turbines*, Risø-R-867(EN).
19. Golubev V., Nguyen L., Mankbadi R., Roger M., Visbal M. (2014), *On flow-acoustic resonant interactions in transitional airfoils*, International Journal of Aeroacoustics, **13**, 1, 1–38, doi: 10.1260/1475-472X.13.1-2.1.
20. Jones L.E., Sandberg R.D. (2011), *Numerical analysis of tonal aerofoil self-noise and acoustic feedback-loops*, Journal of Sound and Vibration, **330**, 6137–6152.
21. Jones L.E., Sandberg R.D., Sandham N.D. (2008), *Direct numerical simulations of forced and unforced separation bubble on an aerofoil at incidence*, Journal of Fluid Mechanics, **602**, 175–207.
22. Jones L.E., Sandberg R.D., Sandham N.D. (2010), *Stability and Receptivity Characteristics of Laminar Separation Bubble on an Aerofoil*, Journal of Fluid Mechanics, **648**, 257–296.
23. Kingan M.J., Pearse J.B. (2009), *Laminar Boundary Layer Instability Noise Produced by an Aerofoil*, Journal of Sound and Vibration, **322**, 808-828.
24. Kurotaki T., Sumi T., Atobe T., Hijama J. (2008), *Numerical simulation around NACA0015 with tonal noise generation*, AIAA Paper 2008-0672.
25. Lighthill M.J. (1952), *On sound generated aerodynamically: I. General theory*, Proceedings of the Royal Society A, **211**, 1107, 564–587, doi: 10.1098/rspa.1952.0060.
26. Lighthill M.J. (1954), *On sound generated aerodynamically: II. Turbulence as a source of sound*, Proceedings of the Royal Society A, **222**, 1148, 1–32, doi: 10.1098/rspa.1954.0049.
27. Mari C., Jeandel D., Mathieu J. (1976), *Methode de calcul de couche limite turbulente compressible avec transfert de chaleur*, International Journal of Heat and Mass Transfer, **19**, 893–899.
28. Mathworks Inc., 2011. Matlab, the Language of Technical Computing Manual.
29. McAlpine A., Nash E.C., Lowson M.V. (1999), *On the generation of discrete frequency tones by the flow around an aerofoil*, Journal of Sound and Vibration, **222**, 753–779.
30. Menter F.R. (1994), *Two-equation eddy-viscosity turbulence models for engineering applications*, AIAA Journal, **32**, 8, 1598–1605.
31. Menter F.R., Langstry R.B., Likki S.R., Suzen Y.B., Huang P.G., Volker S. (2004), *A correlation based transition model using local variables, Part-1, Model Formulation*, ASME-GT2004-53452.
32. Nakano T., Fujisawa N., Lee S. (2006), *Measurement of tonal-noise characteristics and periodic flow structure around NACA0018 aerofoil*, Experiments in Fluids, **40**, 482–490.
33. Nash E.C., Lowson M.V., McAlpine A. (1999), *Boundary layer instability noise on aerofoils*, Journal of Fluid Mechanics, **382**, 27–61.
34. Oerlemans S. (2004), *Wind tunnel aeroacoustic tests of six aerofoils for use on small wind turbines*, National Aerospace Laboratory NLR, NREL/SR-500-35339.
35. Oerlermans S., Migliore P. (2004), *Aeroacoustic wind tunnel tests of wind turbine aerofoils*, AIAA Paper 2004–3042.
36. Paterson R., Vogt P., Fink M., Munch C. (1973), *Vortex noise of isolated aerofoils*, Journal of Aircraft, **10**, 296–302.
37. Plogmann B., Würz W. (2013), *Aeroacoustic measurements on a NACA 0012 applying the Coherent Particle Velocity method*, Experiments in Fluids, **54**, 7, doi: 10.1007/s00348-013-1556-9.
38. Pröbsting S., Scarano F., Morris S.C. (2015), *Regimes of tonal noise on an airfoil at moderate Reynolds number*, Journal of Fluid Mechanics, **780**, 407–438.
39. Rozenberg Y., Roger M., Moureau S. (2008), *Fan blade trailing edge noise prediction using RANS simulation*, Proceedings of the Euronoise Conference, Paris, France.
40. Schlichting H. (1979), *Boundary layer theory*, McGraw Hill.
41. Tam C.K.W., Ju H. (2012), *Aerofoil tones at moderate Reynolds number*, Journal of Fluid Mechanics, **690**, 536–570.
42. Wilcox D.C. (2010), *Turbulence modeling for CFD*, DCW Industries, 3rd Ed.